Exact Riemann problem solutions and upwind fluxes for nonlinear elasticity

V.A. Titarev [a], E. Romenski [b,1] and E. F. Toro [c]

[a,c] University of Trento, Italy
Email: titarev@mail.ru; toro@ing.unitn.it

[b] Cranfield University, MK43 0AL, Cranfield, UK
Email: E.Romenskiy@cranfield.ac.uk

Abstract

The present paper is devoted to the construction and comparative study of upwind methods as applied to the system of one-dimensional nonlinear elasticity equations. We derive a simple approach for building up exact solutions to the Riemann problem and construct a suite of test problems to assess numerical methods. Then we carry out the implementation and a systematic comparative study of some recently proposed simple, upwind fluxes, the focus being on robustness and accurate resolution of delicate features such as linearly degenerate fields.

1 Introduction

The governing equations of nonlinear elasticity constitute a complicated system of hyperbolic conservation laws coupled with an additional differential constrain, the so-called compatibility condition. The classical approach in linear and non-linear elasticity theories, widely accepted by now, consists of second-order systems of differential equations. A different model for inelastic deformations formulated in terms of a first-order hyperbolic system is proposed in [3]. Such a formulation seems to be more appropriate, as it allows the use of well developed mathematical tools for studying various initial-boundary problems; see the recent book [5]. Also, from the computational point of view one may make use of advanced approaches for constructing numerical algorithms to solve the equations approximately, see for instance [20, 7]. The non-linear elasticity equations can be derived from the aforementioned model [3] as a special case. The model from [3] was successfully used in [9, 10] to study wave propagation and high-rate deformations in metals, where the equations, in non-conservative form, were formulated in terms of strain tensor. Conservative formulations in terms of Lagrangian deformation gradient are presented in [15, 13].

[1] On leave from Sobolev Institute of Mathematics, Russian Academy of Sciences, Novosibirsk, Russia

In this paper we adopt as a model for non-linear elasticity, a system of first-order hyperbolic equations in conservation-law form. Modern numerical methods for hyperbolic conservation laws make direct or indirect use of the Riemann problem, e.g. [20, 7]. Developing exact or approximate Riemann solvers for nonlinear elasticity is a difficult task due to the enormous complexity of the system and its associated equation of state. A second-order Godunov-type method based on an approximate Riemann solver is developed in [12]. More recently, an iterative algorithm for the solution of the Riemann problem for general systems of conservation laws was proposed in [11] and an application to one-dimensional elastic equations in terms of Lagrangian deformation gradient was given. These Riemann solvers are quite complex to implement and require a detailed knowledge of the Riemann problem solution. It is therefore desirable to have simpler Godunov-type fluxes to be used in practical computations, which would also be applicable to inelastic media equations.

The present paper is devoted to the construction and comparative study of upwind methods as applied to the one-dimensional system of nonlinear elasticity equations. First we derive a simple method for deriving *exact* solutions to the Riemann problem for non-linear elasticity. The constructed solutions are then proposed as reference solutions to test the performance of numerical methods. These tests include an impact test problem, a separation problem with a sonic point, a test with a stationary contact discontinuity and a conventional shock-tube problem with a structure containing three-waves.

Having established a set of test problems, we carry out a systematic comparative study of some recently proposed Godunov-type fluxes [21, 24, 18, 22] as well as some conventional fluxes such as the centred Lax-Friedrichs flux and a simple linearized Riemann solver. Most of the computations are carried out in the framework of the first-order Godunov method [2]. Particular attention is given to robustness and ability of the methods to accurately resolve delicate features of the solution such as contact waves. Some selected fluxes are also used in the construction of high-order numerical methods in the framework of the weighted essentially non-oscillatory (WENO) schemes [8, 6, 17].

The rest of the paper is organized as follows. In section 2 we give a brief description of the governing equations of nonlinear elasticity. Section 3 is devoted to the construction of exact Riemann problem solutions for some special cases. A description of fluxes is provided in section 4. Section 5 contains first-order numerical results. Higher-order computations on the basis of the WENO method are presented in section 6 and conclusions are drawn in section 7.

2 Governing equations of nonlinear elasticity

2.1 Complete 3D system

Three-dimensional processes of elastic media deformation in the Cartesian coordinate system x_i can be described by the complete set of parameters of state such as the velocity vector $\boldsymbol{u} = \{u_i\}$, Eulerian deformation gradient $C = \{c_{ij}\}$, which we also call the Eulerian distortion tensor, and specific entropy S. Other variables, such as material density ρ, the stress tensor σ_{ik} and the specific internal energy e can be represented as functions of the above parameters.

We formulate the governing equations as a first-order hyperbolic system in conservative form using the Eulerian deformation gradient as the parameter of state. This formulation is a straightforward consequence of the thermodynamically compatible system theory developed in [4, 5]. The system represents momentum, strain and total energy conservation laws and has the following form:

$$\begin{aligned} \frac{\partial \rho u_i}{\partial t} + \frac{\partial (\rho u_i u_k - \sigma_{ik})}{\partial x_k} &= 0, \\ \frac{\partial \rho c_{ij}}{\partial t} + \frac{\partial (\rho c_{ij} u_k - \rho c_{kj} u_i)}{\partial x_k} &= 0, \\ \frac{\partial \rho (e + \boldsymbol{u}^2/2)}{\partial t} + \frac{\partial (\rho u_k (e + \boldsymbol{u}^2/2) - u_i \sigma_{ik})}{\partial x_k} &= 0. \end{aligned} \tag{1}$$

Here we assume summation over repeating indexes. The continuity equation, or mass conservation law, can be derived using the definition of mass density and reads

$$\frac{\partial \rho}{\partial t} + \frac{\partial \rho u_k}{\partial x_k} = 0. \tag{2}$$

This equation can be used for computations instead of one of the equations for distortions c_{ij} in (1).

The closure relation for the system is the equation of state that defines the specific internal energy e as function of distortion tensor and entropy: $e = e(c_{ij}, S)$. Then density ρ, strain tensor g_{ij}, stress tensor σ_{ik} and temperature T are given by

$$\rho = \rho_0 / \det C, \quad G = (g_{ij}) = C^{-1*} C^{-1}, \quad \sigma_{ik} = \rho c_{ij} \frac{\partial e}{\partial c_{kj}} = -2\rho g_{ij} \frac{\partial e}{\partial g_{jk}}, \quad T = \frac{\partial e}{\partial S}.$$

Here ρ_0 is a constant mass density in the reference unstressed state.

For an isotropic medium the equation of state must be a function of three independent invariants I_1, I_2, I_3 of strain tensor which can be chosen in different ways. We shall use

$$I_1 = \mathrm{tr} G = g_{11} + g_{22} + g_{33}, \qquad I_3 = \det G = (\rho/\rho_0)^2,$$

$$I_2 = (g_{11} g_{22} - g_{12} g_{21}) + (g_{22} g_{33} - g_{23} g_{32}) + (g_{33} g_{11} - g_{31} g_{13}).$$

Note that for the two-dimensional case we have to set $g_{33} \equiv 1$. The equation of state used in the present paper is given as the sum of three terms of which two correspond to the hydrodynamic part of the internal energy and one corresponds to the shear deformation [16]:

$$e = \frac{K_0}{2\alpha^2}(I_3^{\alpha/2} - 1)^2 + c_V T_0 I_3^{\gamma/2}(e^{S/c_V} - 1) + \frac{B_0}{2} I_3^{\beta/2}(I_1^2/3 - I_2). \tag{3}$$

Here K_0 and B_0 are bulk and shear modulus, c_V is heat capacity at constant volume, α, β, γ are constants characterizing nonlinear dependence of sound speeds and temperature on the mass density.

Additional steady conservation laws hold for the distortion tensor, which are compatibility conditions and can be easily derived from the conservation equations for c_{ij} from the system (1):

$$\frac{\partial \rho c_{1j}}{\partial x_1} + \frac{\partial \rho c_{2j}}{\partial x_2} + \frac{\partial \rho c_{3j}}{\partial x_3} = 0, \quad j = 1, 2, 3. \tag{4}$$

These equations can be viewed as constrains to be satisfied by solutions of (4).

2.2 Augmented one-dimensional system

Assume that deformation of a medium is uniform along the $x_1 \equiv x$ axis and only one tangential component of the velocity vector is nonzero. In this case the complete set of parameters of state of a medium consists of normal $u = u_1$ and tangential $v = u_2$ components of the velocity vector; $c_{11}, c_{12}, c_{21}, c_{22}$ components of the distortion tensor and entropy S. Consequently, the complete system (1) can be reduced to seven equations. For the purpose of solving the equations numerically it is more convenient to use the continuity equation (2) instead of one of the equations for ρc_{ij}, say ρc_{11}. We therefore adopt the following form of the augmented one-dimensional system:

$$\frac{\partial \boldsymbol{U}}{\partial t} + \frac{\partial \boldsymbol{F}(\boldsymbol{U})}{\partial x} = \boldsymbol{0}. \tag{5}$$

Here the vector of conservative variables $\boldsymbol{U}$ and fluxes $\boldsymbol{F}(\boldsymbol{U})$ are given by

$$\begin{aligned} \boldsymbol{U} &= (\rho, \ \rho u, \ \rho v, \ \rho c_{12}, \ \rho c_{21}, \ \rho c_{22}, \ \rho(E + u^2/2 + v^2/2))^T, \\ \boldsymbol{F}(\boldsymbol{U}) &= (\rho u, \ \rho u^2 - \sigma_{11}, \ \rho uv - \sigma_{21}, \ 0, \ \rho(c_{21}u - c_{11}v)^T, \\ &\qquad \rho(c_{22}u - c_{12}v), \ \rho u(E + (u^2 + v^2)/2) - u\sigma_{11} - v\sigma_{21})^T. \end{aligned} \tag{6}$$

Nonzero components of the strain tensor g_{ij} are

$$g_{11} = f_{11}^2 + f_{21}^2, \quad g_{12} = g_{21} = f_{11}f_{12} + f_{21}f_{22}, \quad g_{22} = f_{12}^2 + f_{22}^2,$$

where the entries f_{ij} of the C^{-1} matrix are given by

$$(f_{11},\ f_{12},\ f_{21},\ f_{22}) = (c_{22}, -c_{12},\ -c_{21}, c_{11})/\mathrm{det}C, \quad \mathrm{det}C = c_{11}c_{22} - c_{12}c_{21}.$$

The mass density can be represented as a function of either c_{ij} or g_{ij}:

$$\rho = \rho_0/\mathrm{det}C = \rho_0\sqrt{g_{11}g_{22} - g_{12}g_{21}}.$$

The components of the stress tensor are given by:

$$\begin{aligned}
\sigma_{11} &= -2\rho g_{11}\frac{\partial E}{\partial g_{11}} - 2\rho g_{12}\frac{\partial E}{\partial g_{21}}, \\
\sigma_{12} = \sigma_{21} &= -2\rho g_{11}\frac{\partial E}{\partial g_{12}} - 2\rho g_{12}\frac{\partial E}{\partial g_{22}}, \\
\sigma_{22} &= -2\rho g_{21}\frac{\partial E}{\partial g_{12}} - 2\rho g_{22}\frac{\partial E}{\partial g_{22}}.
\end{aligned}$$

Finally, we note that the compatibility conditions (4) in the one-dimensional case read as follows:

$$\rho c_{11} = \mathrm{const}, \quad \rho c_{12} = \mathrm{const}. \tag{7}$$

2.3 Eigenstructure of the system

We analyze the eigenstructure of the one-dimensional system (5), (6). To do so we write it in quasi-linear form for the vector of primitive variables $\boldsymbol{W} = (u, v, c_{11}, c_{12}, c_{21}, c_{22}, S)$:

$$\frac{\partial \boldsymbol{W}}{\partial t} + \boldsymbol{A}(\boldsymbol{W})\frac{\partial \boldsymbol{W}}{\partial x} = \boldsymbol{0}, \tag{8}$$

where the matrix $\boldsymbol{A}(\boldsymbol{W})$ is given by

$$\boldsymbol{A} = \begin{pmatrix}
u & 0 & -A_{1111} & -A_{1112} & -A_{1121} & -A_{1122} & -A_{110} \\
0 & u & -A_{2111} & -A_{2112} & -A_{2121} & -A_{2122} & -A_{210} \\
-c_{11} & 0 & u & 0 & 0 & 0 & 0 \\
-c_{12} & 0 & 0 & u & 0 & 0 & 0 \\
0 & -c_{11} & 0 & 0 & u & 0 & 0 \\
0 & -c_{12} & 0 & 0 & 0 & u & 0 \\
0 & 0 & 0 & 0 & 0 & 0 & u
\end{pmatrix}$$

with

$$A_{ijkl} = \frac{1}{\rho}\frac{\partial \sigma_{ij}}{\partial c_{kl}}, \quad A_{ij0} = \frac{1}{\rho}\frac{\partial \sigma_{ij}}{\partial S}.$$

The eigenvalues of A can be found as the roots of the equation

$$(u-\lambda)^3((u-\lambda)^4 - K_2(u-\lambda)^2 + K_0) = 0, \tag{9}$$

where the coefficients K_0, K_2 are given by

$$K_2 = c_{11}(A_{1111} + A_{2121}) + c_{12}(A_{1112} + A_{2122}),$$

$$K_0 = c_{11}^2 \begin{vmatrix} A_{1111} & A_{1121} \\ A_{2111} & A_{2121} \end{vmatrix} + c_{11}c_{12} \left(\begin{vmatrix} A_{1111} & A_{1122} \\ A_{2111} & A_{2122} \end{vmatrix} + \begin{vmatrix} A_{1112} & A_{1121} \\ A_{2112} & A_{2121} \end{vmatrix} \right) + c_{12}^2 \begin{vmatrix} A_{1112} & A_{1122} \\ A_{2112} & A_{2122} \end{vmatrix}.$$

This gives us the following set of eigenvalues:

$$\lambda_1 = u - \sqrt{x}_1, \quad \lambda_2 = u - \sqrt{x}_2, \quad \lambda_3 = \lambda_4 = \lambda_5 = u, \quad \lambda_6 = u + \sqrt{x}_2, \quad \lambda_7 = u + \sqrt{x}_1.$$

where

$$x_1 = \frac{1}{2}(K_2 + \sqrt{K_2^2 - 4K_0})/2, \quad x_2 = \frac{1}{2}(K_2 - \sqrt{K_2^2 - 4K_0})$$

The right eigenvectors are given by:

$$\boldsymbol{r}_1 = \frac{1}{2} \begin{pmatrix} (Q^{-1}D_\Lambda^{-1})_{11} \\ (Q^{-1}D_\Lambda^{-1})_{21} \\ c_{11}(Q^{-1}D_\Lambda^{-2})_{11} \\ c_{12}(Q^{-1}D_\Lambda^{-2})_{11} \\ c_{11}(Q^{-1}D_\Lambda^{-2})_{21} \\ c_{12}(Q^{-1}D_\Lambda^{-2})_{21} \\ 0 \end{pmatrix}, \quad \boldsymbol{r}_2 = \frac{1}{2} \begin{pmatrix} (Q^{-1}D_\Lambda^{-1})_{12} \\ (Q^{-1}D_\Lambda^{-1})_{22} \\ c_{11}(Q^{-1}D_\Lambda^{-2})_{12} \\ c_{12}(Q^{-1}D_\Lambda^{-2})_{12} \\ c_{11}(Q^{-1}D_\Lambda^{-2})_{22} \\ c_{12}(Q^{-1}D_\Lambda^{-2})_{22} \\ 0 \end{pmatrix}, \quad \boldsymbol{r}_7 = \frac{1}{2} \begin{pmatrix} (Q^{-1}D_\Lambda^{-1})_{12} \\ (Q^{-1}D_\Lambda^{-1})_{22} \\ -c_{11}(Q^{-1}D_\Lambda^{-2})_{12} \\ -c_{12}(Q^{-1}D_\Lambda^{-2})_{12} \\ -c_{11}(Q^{-1}D_\Lambda^{-2})_{22} \\ -c_{12}(Q^{-1}D_\Lambda^{-2})_{22} \\ 0 \end{pmatrix},$$

$$\boldsymbol{r}_3 = \begin{pmatrix} 0 \\ 0 \\ c_{11}(\Lambda_{11}^{-1}A_{1112} + \Lambda_{12}^{-1}A_{2112}) \\ c_{12}(\Lambda_{11}^{-1}A_{1112} + \Lambda_{12}^{-1}A_{2112}) - 1 \\ c_{11}(\Lambda_{21}^{-1}A_{1112} + \Lambda_{22}^{-1}A_{2112}) \\ c_{12}(\Lambda_{21}^{-1}A_{1112} + \Lambda_{22}^{-1}A_{2112}) \\ 0 \end{pmatrix}, \quad \boldsymbol{r}_4 = \begin{pmatrix} 0 \\ 0 \\ c_{11}(\Lambda_{11}^{-1}A_{1122} + \Lambda_{12}^{-1}A_{2122}) \\ c_{12}(\Lambda_{11}^{-1}A_{1122} + \Lambda_{12}^{-1}A_{2122}) \\ c_{11}(\Lambda_{21}^{-1}A_{1122} + \Lambda_{22}^{-1}A_{2122}) \\ c_{12}(\Lambda_{21}^{-1}A_{1122} + \Lambda_{22}^{-1}A_{2122}) - 1 \\ 0 \end{pmatrix}$$

$$\boldsymbol{r}_5 = \begin{pmatrix} 0 \\ 0 \\ -c_{11}(\Lambda_{11}^{-1}A_{110} + \Lambda_{12}^{-1}A_{210}) \\ -c_{12}(\Lambda_{11}^{-1}A_{110} + \Lambda_{12}^{-1}A_{210}) \\ -c_{11}(\Lambda_{21}^{-1}A_{110} + \Lambda_{22}^{-1}A_{210}) \\ -c_{12}(\Lambda_{21}^{-1}A_{110} + \Lambda_{22}^{-1}A_{210}) \\ 1 \end{pmatrix} \quad \boldsymbol{r}_6 = \frac{1}{2} \begin{pmatrix} (Q^{-1}D_\Lambda^{-1})_{11} \\ (Q^{-1}D_\Lambda^{-1})_{21} \\ -c_{11}(Q^{-1}D_\Lambda^{-2})_{11} \\ -c_{12}(Q^{-1}D_\Lambda^{-2})_{11} \\ -c_{11}(Q^{-1}D_\Lambda^{-2})_{21} \\ -c_{12}(Q^{-1}D_\Lambda^{-2})_{21} \\ 0 \end{pmatrix},$$

The left eigenvectors are given by

$$\begin{aligned}
\boldsymbol{l}_1 &= ((D_\Lambda Q)_{11},\ (D_\Lambda Q)_{12},\ Q_{11}A_{1111} + Q_{12}A_{2111},\ Q_{11}A_{1112} + Q_{12}A_{2112},\\
&\qquad Q_{11}A_{1121} + Q_{12}A_{2121},\ Q_{11}A_{1122} + Q_{12}A_{2122},\ Q_{11}A_{110} + Q_{12}A_{210})\\
\boldsymbol{l}_2 &= ((D_\Lambda Q)_{21}, (D_\Lambda Q)_{22}, Q_{21}A_{1111} + Q_{22}A_{2111}, Q_{21}A_{1112} + Q_{22}A_{2112},\\
&\qquad Q_{21}A_{1121} + Q_{22}A_{2121}, Q_{21}A_{1122} + Q_{22}A_{2122}, Q_{21}A_{110} + Q_{22}A_{210})\\
\boldsymbol{l}_3 &= (0, 0, c_{12}/c_{11}, -1, 0, 0, 0)\\
\boldsymbol{l}_4 &= (0, 0, 0, c_{12}/c_{11}, -1, 0, 0)\\
\boldsymbol{l}_5 &= (0, 0, 0, 0, 0, 0, 1)\\
\boldsymbol{l}_6 &= ((D_\Lambda Q)_{11}, (D_\Lambda Q)_{12}, -Q_{11}A_{1111} - Q_{12}A_{2111}, -Q_{11}A_{1112} - Q_{12}A_{2112},\\
&\qquad -Q_{11}A_{1121} - Q_{12}A_{2121}, -Q_{11}A_{1122} - Q_{12}A_{2122}, -Q_{11}A_{110} - Q_{12}A_{210})\\
\boldsymbol{l}_7 &= ((D_\Lambda Q)_{21}, (D_\Lambda Q)_{22}, -Q_{21}A_{1111} - Q_{22}A_{2111}, -Q_{21}A_{1112} - Q_{22}A_{2112},\\
&\qquad -Q_{21}A_{1121} - Q_{22}A_{2121}, -Q_{21}A_{1122} - Q_{22}A_{2122}, -Q_{21}A_{110} - Q_{22}A_{210})
\end{aligned}$$

Here $\boldsymbol{\Lambda}$ is a second order symmetric matrix

$$\boldsymbol{\Lambda} = \begin{pmatrix} A_{1111} & A_{1112} & A_{1121} & A_{1122} \\ A_{2111} & A_{2112} & A_{2121} & A_{2122} \end{pmatrix} \begin{pmatrix} c_{11} & 0 \\ c_{12} & 0 \\ 0 & c_{11} \\ 0 & c_{12} \end{pmatrix},$$

which is called the acoustic matrix and admits a factorization

$$\Lambda = \boldsymbol{A}\boldsymbol{P} = \boldsymbol{Q}^{-1}\boldsymbol{D}_\Lambda^2\boldsymbol{Q}, \quad \boldsymbol{D}_\Lambda = \mathrm{diag}(\sqrt{x}_1, \sqrt{x}_2),$$

where $\boldsymbol{Q}$ is an orthogonal matrix; Λ_{ij}^{-1} denotes (i,j) element of the inverse matrix $\Lambda^{-1} = \boldsymbol{Q}^{-1}D_\Lambda^{-2}\boldsymbol{Q}$.

It can be seen that there are three linearly degenerate fields corresponding to $\lambda = u$ and four nonlinear fields.

3 Exact Riemann problem solutions

In this section we develop a procedure for constructing exact solutions to the local Riemann problem, which is the Cauchy problem for (5) with piece-wise constant initial data of the form

$$\boldsymbol{U}(x,0) = \begin{cases} \boldsymbol{U}_L, & x < 0, \\ \boldsymbol{U}_R, & x > 0. \end{cases} \tag{10}$$

We consider two special cases: an isolated contact discontinuity with possible changes in all components of the vector of primitive variables $\boldsymbol{W}$ and the purely one-dimensional shock-tube problem, in which no disturbances in the transverse direction exist.

3.1 Isolated contact discontinuity

The Rankine-Hugoniot relations connecting the left and right states through a discontinuity moving with velocity D are given by

$$\begin{aligned}
[\rho u]D &= [\rho u^2 - \sigma_{11}], \\
[\rho v]D &= [\rho uv - \sigma_{21}], \\
[\rho c_{11}]D &= 0, \\
[\rho c_{12}]D &= 0, \\
[\rho c_{21}]D &= [\rho c_{21}u - \rho c_{11}v], \\
[\rho c_{22}]D &= [\rho c_{22}u - \rho c_{12}v], \\
[\rho(e + (u^2+v^2)/2)]D &= [\rho u(e + (u^2+v^2)/2) - u\sigma_{11} - v\sigma_{21}],
\end{aligned}$$

where for any quantity $[\phi] = \phi_R - \phi_L$. An isolated contact discontinuity is defined by the condition that the normal velocity component does not change across it:

$$u_L = u_R = D.$$

Assume that the right state $\boldsymbol{W}_R$ and one component of $\boldsymbol{W}_L$, say entropy, are given. Then, taking into account the compatibility conditions (7), we obtain the following five equations for the remaining unknown quantities $(v,\ c_{11},\ c_{12},\ c_{21},\ c_{22})$ of the left state $\boldsymbol{W}_L$:

$$[v] = [\sigma_{11}] = [\sigma_{21}] = [\rho c_{11}] = [\rho c_{12}] = 0 \tag{11}$$

The nonlinear system (11) can be solved by means of the Newton method.

3.2 Complete solution for the purely one-dimensional case

Let us assume that v, c_{12}, c_{21} and c_{22} are constant in the initial data. Then the structure of the solution is similar to that of the ideal Euler equations, and consists of three distinct waves: a left nonlinear wave, associated with λ_1, a contact discontinuity, associated with λ_3 and a right nonlinear wave, associated with λ_7. These three waves separate four constant states, which are from left to right are: $\boldsymbol{W}_L$, $\boldsymbol{W}_{*L}$, $\boldsymbol{W}_{*R}$ and $\boldsymbol{W}_R$. The left nonlinear wave can be either a rarefaction wave occupying the region

$$\lambda_{1L} = \lambda_1(\boldsymbol{W}_L) \le x/t \le S_L = \lambda_1(\boldsymbol{W}_{*L})$$

in $x-t$ space or a shock wave moving the speed S_L so that across it we have the Rankine - Hugoniot conditions:

$$\boldsymbol{F}_L - \boldsymbol{F}_{*L} = S_L\left(\boldsymbol{U}_L - \boldsymbol{U}_{*L}\right). \tag{12}$$

Similarly, the right wave is either a rarefaction

$$S_R = \lambda_7(\boldsymbol{W}_{*R}) \leq x/t \leq \lambda_7(\boldsymbol{W}_R) = \lambda_{7R}$$

or a shock moving with the speed S_R:

$$\boldsymbol{F}_R - \boldsymbol{F}_{*R} = S_R\left(\boldsymbol{U}_R - \boldsymbol{U}_{*R}\right). \tag{13}$$

The middle wave of velocity S_M is always a contact discontinuity dividing the unknown star region between nonlinear waves into two adjacent subregions: star left $\boldsymbol{W}_{*L}$ and star right $\boldsymbol{W}_{*R}$. Consequently, there exist four possible wave patterns.

The solution to the Riemann problem is completely defined once we now S_L, S_R and the type of the nonlinear waves. Moreover, the left star state is a function of S_L and $\boldsymbol{W}_L$, whereas the right star state is a function of S_R and $\boldsymbol{W}_R$:

$$\boldsymbol{W}_{*L} = \boldsymbol{W}_{*L}(S_L, \boldsymbol{W}_L), \quad \boldsymbol{W}_{*R} = \boldsymbol{W}_{*L}(S_R, \boldsymbol{W}_R).$$

The solution procedure developed here uses the fact that across the middle contact wave both normal velocity $u_* = S_M$ and normal stress σ_{11} are constant. This gives us a nonlinear system of two equations for the unknown velocities S_L, S_R of the outer nonlinear waves:

$$\begin{aligned} f_1(S_L, S_R) &= u(\boldsymbol{W}_{*L}) - u(\boldsymbol{W}_{*R}) = 0, \\ f_2(S_L, S_R) &= \sigma_{11}(\boldsymbol{W}_{*L}) - \sigma_{11}(\boldsymbol{W}_{*R}) = 0. \end{aligned} \tag{14}$$

We now proceed to establish the expressions for computing the left and right star states as functions of S_L and S_R. Consider first the left wave. If this wave is a rarefaction we have the following system of ordinary differential equations valid across this wave [14]:

$$\frac{d}{d\xi}\boldsymbol{W} = \frac{\boldsymbol{r}_1}{(\boldsymbol{r}_1, \nabla_w \lambda_1(\boldsymbol{W}))}, \quad \lambda_{1L} \leq \xi \leq S_L \tag{15}$$

coupled with the initial condition $\boldsymbol{W}(\lambda_{1L}) = \boldsymbol{W}_L$. Here ∇_w denotes the gradient operator with respect to components of the vector of primitive variables $\boldsymbol{W}$. The sought left star state is given by the solution of (15) evaluated at $\xi = S_L$.

If the left wave happens to be a shock with the velocity S_L, then the left star value is given by the Rankine – Hugoniot conditions (12). The nonlinear system for the left star conservative variable $\boldsymbol{U}_{*L}$ is solved numerically using the Newton iteration method.

The derivation of $\boldsymbol{W}_{*R}$ as a function of S_R is carried out in an entirely analogous manner. If the wave is a rarefaction then across it we have:

$$\frac{d}{d\xi}\boldsymbol{W} = \frac{\boldsymbol{r}_7}{(\boldsymbol{r}_7, \nabla_w \lambda_7(\boldsymbol{W}))}, \quad S_R \leq \xi \leq \lambda_{7R} \tag{16}$$

coupled with the initial condition $\boldsymbol{W}(\lambda_{7R}) = \boldsymbol{W}_R$. Note that we solve (16) from right to left. If instead the wave is a shock, we have the nonlinear system (13) for the right star conservative variable $\boldsymbol{U}_{*R}$.

Overall, the solution algorithm produces a sequence of approximations to the star values $\boldsymbol{W}_{*L}^{(n)}$, $\boldsymbol{W}_{*R}^{(n)}$, where n is the number of the current iteration, as follows. We use the Newton method to solve (14). Knowing $\boldsymbol{W}_{*L}^{(n)}$, $\boldsymbol{W}_{*R}^{(n)}$ we find out the type of the nonlinear waves present in the solution by analyzing the inclination of characteristics. If they converge, then the wave is a compressive wave, a shock. Otherwise we have a rarefaction wave. Having established the type of waves we can compute the star values and find the next approximation to S_L, S_R from the following linear system:

$$\begin{pmatrix} S_L^{(n+1)} \\ S_R^{(n+1)} \end{pmatrix} = \begin{pmatrix} S_L^{(n)} \\ S_R^{(n)} \end{pmatrix} - \begin{pmatrix} \dfrac{\partial f_1}{\partial S_L}\left(S_L^{(n)}, S_R^{(n)}\right) & \dfrac{\partial f_1}{\partial S_R}\left(S_L^{(n)}, S_R^{(n)}\right) \\ \dfrac{\partial f_2}{\partial S_L}\left(S_L^{(n)}, S_R^{(n)}\right) & \dfrac{\partial f_2}{\partial S_R}\left(S_L^{(n)}, S_R^{(n)}\right) \end{pmatrix}^{-1} \begin{pmatrix} f_1\left(S_L^{(n)}, S_R^{(n)}\right) \\ f_2\left(S_L^{(n)}, S_R^{(n)}\right)) \end{pmatrix}.$$

What is left is to describe the procedure for finding an initial guess value for the star states $\boldsymbol{W}_{*L}$, $\boldsymbol{W}_{*R}$ and the velocities S_L, S_R. Unfortunately, unlike the Euler equations, the nonlinear elasticity equations do not lend themselves easily to analytical construction of initial guess values. It appears as if the only possibility is to use the linearized solver, described below in section 4, to produce approximations to $\boldsymbol{W}_{*L}$, $\boldsymbol{W}_{*R}$. Although this works well for a wide class of initial data, the linearized solver fails for some special situations, see section of numerical results. However, since our goal is to use the exact Riemann solver in the construction of reference exact solutions rather than as a local solver in the numerical scheme, the initial approximation can be found by using the results of some first-order dissipative scheme run on a sufficiently fine mesh.

4 Numerical fluxes for finite-volume methods

Consider now a control volume in $x-t$ space of dimensions $\Delta x = x_{i+1/2} - x_{i-1/2}$, $\Delta t = t^{n+1} - t^n$. A finite volume method for solving (5) reads as follows:

$$\boldsymbol{U}_i^{n+1} = \boldsymbol{U}_i^n - \frac{\Delta t}{\Delta x}\left(\boldsymbol{F}_{i+1/2} - \boldsymbol{F}_{i-1/2}\right), \tag{17}$$

where $\boldsymbol{U}_i^n$ is an approximation to the cell average and $\boldsymbol{F}_{i+1/2}$ is the numerical flux. The description of the scheme (17) is complete once expressions for the numerical fluxes are provided. Godunov [2] proposed to use the self-similar solution $\boldsymbol{U}_*(x/t)$ of the Riemann problem (5),(10) with the initial data $\boldsymbol{U}_L = \boldsymbol{U}_i$, $\boldsymbol{U}_R = \boldsymbol{U}_{i+1}$ to compute numerical fluxes in the direction normal to the cell faces. The original Godunov flux is given by $\boldsymbol{F}_{i+1/2} = \boldsymbol{F}(\boldsymbol{U}_*(0))$. More generally, the numerical flux can be defined as a two-point function of left and right data in the local Riemann problem, namely

$$\boldsymbol{F}_{i+1/2} = \boldsymbol{F}_{i+1/2}(\boldsymbol{U}_L, \boldsymbol{U}_R). \tag{18}$$

In most cases the upwind Godunov-type fluxes cannot be written as an explicit function of $\boldsymbol{U}_L$, $\boldsymbol{U}_R$. Centred fluxes can be written in the form (18), which makes them simple to implement but also rather diffusive as compared to upwind fluxes.

We now deal with different upwind fluxes that can be used as the building block for non-oscillatory advection schemes.

4.1 Linearized Riemann solver

An upwind flux is constructed here by using a simple linearized Riemann solver obtained by freezing the matrix A in (8) at the average state

$$\boldsymbol{W}_0 = (\boldsymbol{W}_L + \boldsymbol{W}_R)/2$$

and considering the corresponding linear hyperbolic system:

$$\frac{\partial \boldsymbol{W}}{\partial t} + \boldsymbol{A}_0 \frac{\partial \boldsymbol{W}}{\partial x} = \boldsymbol{0}, \quad A_0 = A(\boldsymbol{W}_0) \tag{19}$$

The self-similar solution $\boldsymbol{W}_*(x/t)$ of (19) (and thus $\boldsymbol{U}_*(x/t)$) can be easily constructed since we know the eigenvectors and eigenvalues. The flux is then given by $\boldsymbol{F}(\boldsymbol{U}_*(0))$.

The availability of the linearized solver is important for a number of reasons. Firstly, it can be used as a local solver for a class of problems of nonlinear elasticity. It recognizes all waves in the solution and is thus accurate for delicate features such as contact discontinuities. Secondly, the knowledge of eigenvectors is necessary for the construction of high-order methods which use the reconstruction procedure in characteristic variables. Thirdly, the linearized Riemann solver is an essential element for the EVILIN flux [22] described below.

However, conventional linearized Riemann solvers have a number of deficiencies. Firstly, they may lack robustness at strong shock waves. Secondly, they fail to compute sonic points correctly giving a large unphysical jump in all flow variables, a *rarefaction shock*, unless explicit *entropy fixes* are enforced. Finally, the linearized Riemann solvers cannot handle the situation when the Riemann problem solution contains very strong rarefaction waves [1]. Therefore, the linearized solver is not generally recommended for practical applications except for some special situations.

4.2 FORCE and generalized FORCE fluxes

Two classical centred fluxes are the Lax-Friedrichs flux

$$\boldsymbol{F}^{LF}_{i+\frac{1}{2}}(\boldsymbol{U}_L, \boldsymbol{U}_R, \Delta t, \Delta x) = \frac{1}{2}[\boldsymbol{F}(\boldsymbol{U}_L) + \boldsymbol{F}(\boldsymbol{U}_R)] - \frac{1}{2}\frac{\Delta x}{\Delta t}[\boldsymbol{U}_R - \boldsymbol{U}_L] \tag{20}$$

and the two-step Lax-Wendroff flux

$$\boldsymbol{F}^{LW}_{i+\frac{1}{2}}(\boldsymbol{U}_L,\boldsymbol{U}_R,\Delta t,\Delta x)=\boldsymbol{F}(\boldsymbol{U}_{LW})\ ,\ \ \boldsymbol{U}_{LW}=\frac{1}{2}[\boldsymbol{U}_L+\boldsymbol{U}_R]-\frac{1}{2}\frac{\Delta t}{\Delta x}[\boldsymbol{F}(\boldsymbol{U}_R)-\boldsymbol{F}(\boldsymbol{U}_L)]\ . \quad (21)$$

Another, more recent, first order centred flux is the FORCE flux [19, 23] given by the arithmetic average of the Lax-Friedrichs and Lax-Wendroff fluxes:

$$\boldsymbol{F}^{\text{force}}_{i+\frac{1}{2}}(\boldsymbol{U}_L,\boldsymbol{U}_R,\Delta t,\Delta x)=\frac{1}{2}\boldsymbol{F}^{LW}_{i+\frac{1}{2}}(\boldsymbol{U}_L,\boldsymbol{U}_R,\Delta t,\Delta x)+\frac{1}{2}\boldsymbol{F}^{LF}_{i+\frac{1}{2}}(\boldsymbol{U}_L,\boldsymbol{U}_R,\Delta t,\Delta x). \quad (22)$$

As is well known, centred (or symmetric) fluxes contain no explicit wave propagation information which makes them simple, efficient and applicable to very complex equations, but also quite diffusive and dependent on the Courant number coefficient. In particular, waves associated with linearly degenerate fields, such as contact waves, shear waves and vortices, are poorly resolved.

A simple way of removing the dependence of the truncation error on the reciprocal of the Courant number in the FORCE flux while retaining its simplicity is to use a local time step in (22); this time step is estimated from the data $\boldsymbol{U}_L$, $\boldsymbol{U}_R$ [18]. A further improvement is the generalized FORCE (GFORCE) flux [24], which is given by a convex average of (20) and (21), again with the local selection of the time step:

$$\boldsymbol{F}^{GF}_{i+\frac{1}{2}}(\boldsymbol{U}_L,\boldsymbol{U}_R)=\omega\boldsymbol{F}^{LW}_{i+\frac{1}{2}}(\Delta t_g,\Delta x_g)+(1-\omega)\boldsymbol{F}^{LF}_{i+\frac{1}{2}}(\Delta t_g,\Delta x_g),\quad \omega=\frac{1}{1+K_g}. \quad (23)$$

Here $0<K_g\leq 1$ is a prescribed local Courant number coefficient; usually we take $K_g=0.9$. The choice $\Omega=1/2$ gives the modified FORCE flux of [18]. The time step used in the evaluation of the flux is computed from the initial data $\boldsymbol{U}_L$, $\boldsymbol{U}_R$ as

$$\Delta t_g=K_g\Delta x_g/S_{max}. \quad (24)$$

Here S_{max} is the speed of the fastest wave in the local solution. The local cell size Δx_g can be chosen arbitrary due to the self-similar structure of the solution of the conventional Riemann problem. For example, one could take $\Delta x_g\equiv 1$ or $\Delta x_g\equiv\Delta x$. Note, that generally speaking $\Delta t_g\neq\Delta t$.

The GFORCE flux is upwind due to the fact that the nonlinear weight ω in (23) depends on the local wave speed. For the linear advection equation with constant coefficient the proposed flux (23) reproduces the Godunov's upwind flux.

4.3 GMUSTA and EVILIN Riemann solvers

The idea of the multi-stage (MUSTA) Riemann solver [21] is to obtain an upwind numerical flux by evolving in time the initial data in the local Riemann problem. Below we briefly outline the generalized version of MUSTA, called GMUSTA, as given in [21, 18, 24].

Let us introduce a separate (local) spatial domain and corresponding mesh with $2M$ cells: $-M+1 \le m \le M$ and cell size δx. The boundary between cells $m=0$ and $m=1$ corresponds to the interface position $x=0$ in (10). Transmissive boundary conditions are applied at numerical boundaries $x_{\pm M+1/2}$ on the grounds that the Riemann - like data extends to $\pm\infty$. We now want to solve this Riemann problem numerically on a given separate mesh and construct a sequence of *evolved* data states $\boldsymbol{Q}_m^{(l)}$, $0 \le l \le k$ in such a way, that the final values $\boldsymbol{Q}_0^{(k)}$, $\boldsymbol{Q}_1^{(k)}$ adjacent to the origin are close to the sought Godunov state. Here k is the total number of stages (time steps) on this separate mesh of the algorithm.

The GMUSTA time marching for $m=-M+1,\dots M$ is organized by using the first-order scheme with the GFORCE flux (23) on the chosen separate mesh:

$$\boldsymbol{U}_m^{(l+1)} = \boldsymbol{U}_m^{(l)} - \frac{\delta t}{\delta x}\left(\boldsymbol{F}_{m+1/2}^{(l)} - \boldsymbol{F}_{m-1/2}^{(l)}\right), \quad \boldsymbol{F}_{m+1/2}^{(l)} = \boldsymbol{F}^{GF}(\boldsymbol{U}_m^{(l)}, \boldsymbol{U}_{m+1}^{(l)}). \tag{25}$$

The time marching procedure is stopped when the required number of stages k is reached. At the final stage we have a pair of values adjacent to the interface position. For the construction of Godunov-type advection schemes one needs a numerical flux at the origin, which for the outlined procedure is given by

$$\boldsymbol{F}_{i+1/2}^{GM} = \boldsymbol{F}_{1/2}^{(k)} = \boldsymbol{F}^{GF}(\boldsymbol{U}_0^{(k)}, \boldsymbol{U}_1^{(k)}). \tag{26}$$

The cell size δx can be chosen arbitrarily due to the self-similar structure of the solution of the conventional Riemann problem. Normally we take $\delta x \equiv 1$. The Courant number coefficient K_{musta} is prescribed by the user; we typically take $K_{musta} = 9/10$. The time step δt is computed from the data $\boldsymbol{U}_m^{(l)}$ according to the conventional formula

$$\delta t = K_{musta}\delta x / S_{max}.$$

with the only difference that S_{max} is computed from all cells in the GMUSTA mesh.

The EVILIN Riemann solver [22] is a variant of GMUSTA which uses GMUSTA time marching as a predictor and a linearized Riemann solver as a corrector. The EVILIN flux is constructed by applying the linearized solver to the states adjacent to the origin, namely $\boldsymbol{Q}_0^{(k)}$, $\boldsymbol{Q}_1^{(k)}$, which are obtained by the GMUSTA time marching. To this end we solve exactly the following linearized Riemann problem:

$$\begin{aligned} &\partial_t \boldsymbol{U} + \boldsymbol{A}_{1/2}\partial_x \boldsymbol{U} = \boldsymbol{0}, \quad \boldsymbol{A}_{1/2} = \boldsymbol{A}\left(\tfrac{1}{2}(\boldsymbol{U}_0^{(k)} + \boldsymbol{Q}_1^{(k)})\right) \\ &\boldsymbol{U}(x,0) = \begin{cases} \boldsymbol{U}_0^{(k)} & \text{if} \quad x<0\,, \\ \boldsymbol{U}_1^{(k)} & \text{if} \quad x>0\,. \end{cases} \end{aligned} \tag{27}$$

The aim of EVILIN is to retain the good resolution of the linearized solver and while avoiding its limitations. We note that the usual shortcomings of linearized Riemann

solvers are not present with EVILIN. This is due to the fact that we apply the linearized Riemann solver to *evolved* values rather than to the initial data. See [22] for more details and numerical examples.

5 First-order numerical results

In this section we present a comparative study of the described numerical fluxes as implemented in the first-order finite volume framework. As test problems we solve Riemann problems with piece-wise constant initial data defined in a computational domain $[0:1]$:

$$\frac{\partial \boldsymbol{U}}{\partial t} + \frac{\partial \boldsymbol{F}(\boldsymbol{U})}{\partial x} = 0, \quad \boldsymbol{W}(x,0) = \begin{cases} \boldsymbol{W}_L, & x < x_0 \ , \\ \boldsymbol{W}_R, & x > x_0 \ , \end{cases} \tag{28}$$

where x_0 is the position of the discontinuity in initial data. Note that we specify initial data in terms of primitive variables rather than conservative ones to make the presentation more convenient. Transmissive boundary conditions are applied at $x = 0$ and $x = 1$. As the material for test computations we take copper with the following constants in the equation of state:

$$\rho_0 = 8.9 \ g/cm^3, \ K_0 = c_0^2 - \frac{4}{3} b_0^2, \ B_0 = b_0^2, \ c_0 = 0.46 \ cm/ms, \ b_0 = 0.21 \ cm/ms,$$

$$T_0 = 300 \ K, \ c_v = 0.4 \cdot 10^{-4} \ \frac{g}{ms \ K}, \ \alpha = 1.0, \ \beta = 3.0, \ \gamma = 2.0.$$

In all calculations we denote the GMUSTA and EVILIN Riemann solvers with k stages as GMUSTA-k and EVILIN-k, respectively. Symbols correspond to numerical solution of the method under discussion. Unless otherwise specified, the solid line corresponds to the exact solution obtained using the methods from the previous section.

5.1 Impact test problem

We solve the Riemann problem with the initial data corresponding to two colliding regions:

$$\boldsymbol{W}_L = (+5, 0, 1, 0, 0, 1, 0), \quad \boldsymbol{W}_R = (-5, 0, 1, 0, 0, 1, 0), \quad x_0 = 0.5. \tag{29}$$

The exact solution consists of two shock waves of velocities $S = \pm 11.1$ and a constant star state

$$\boldsymbol{W}_{*L} = \boldsymbol{W}_{*R} = \boldsymbol{W}_* = (0.0, 0, 0.6894, 0, 0, 1, 0.0014)$$

and is given by

$$\boldsymbol{W}(x,t) = \begin{cases} \boldsymbol{W}_L, & & (x - x_0)/t & < -S \ , \\ \boldsymbol{W}_*, & -S < & (x - x_0)/t & < S \ , \\ \boldsymbol{W}_R, & & (x - x_0)/t & > S \ . \end{cases}$$

We run the schemes up to the output time $t = 0.03$ on a mesh of 100 cells with a CFL coefficient $CFL = 0.9$. Figs. 1 – 3 show computed results for Lax-Friedrichs, GFORCE and EVILIN fluxes. The solid line corresponds to the exact solution. We show density and the stress component σ_{22}. Other quantities such as normal velocity u and normal stress σ_{11} are computed satisfactorily by all methods. The results of GMUSTA-1 are very similar to those of GFORCE and are thus omitted. The linearized solver fails for this problem and hence no solution is shown.

We see that the shock wave positions are computed correctly by all methods, the only difference being the resolution of the fronts. The main error, however, is committed in the star region around the (trivial) contact wave, where non-physical under- and overshoots in ρ and σ_{22} are produced by all methods. Overall, the scheme with the GFORCE flux is the most accurate. We also note large over and undershoots near the contact wave present in the result of the EVILIN-1 flux.

5.2 Symmetric separation test problem

We solve the Riemann problem with the following symmetric initial data, corresponding to the separation of two regions of velocity V:

$$\boldsymbol{W}_L = (-0.75, 0, 1, 0, 0, 1, 0), \quad \boldsymbol{W}_R = (+0.75, 0, 1, 0, 0, 1, 0), \tag{30}$$

and $x_0 = 0.5$. The self-similar solution to the problem consists of two rarefaction waves and a constant star state. We remark that for such problems linearized Riemann solvers fail provided the separation velocity is large enough. The star state and the complete solution are given by

$$\boldsymbol{W}_* = (0, 0, 1.291, 0, 0, 1, 0),$$

$$\boldsymbol{W}(x,t) = \begin{cases} \boldsymbol{W}_L, & (x-x_0)/t < -5.35, \\ \text{left rarefaction}, & -5.35 < (x-x_0)/t < -1.5888, \\ \boldsymbol{W}_*, & -1.5888 < (x-x_0)/t < 1.5888 \\ \text{right rarefaction}, & -1.5888 < (x-x_0)/t < 5.35, \\ \boldsymbol{W}_R, & (x-x_0)/t > 5.350. \end{cases}$$

For a given x/t the value of $\boldsymbol{W}$ inside rarefaction waves can be obtained by integrating (15) for the left wave and (16) for the right wave. It is obvious that this test problem is exceedingly difficult due to the presence of huge deformations of the material.

We run the schemes up to the output time $t = 0.07$ with CFL coefficient $CFL = 0.9$. A mesh of 100 cells is used. For the given separation velocity both the linearized solver

and EVILIN fail. In particular, the EVILIN solver fails for any practical number of stages. Fig. 4 shows results of Lax-Friedrichs and GMUSTA-1 fluxes. The results of GFORCE are somewhat more diffusive than GMUSTA-1 and are thus omitted. We see that both Lax-Friedrichs and GMUSTA-1 produce rather inaccurate results. The most visible artifact is a deep in density and stress in the star region. When the mesh is refined this deep slowly disappears.

Finally we note, that for sufficiently large values of the separation velocity in the initial data all methods fail, including the Lax-Friedrichs flux, even though the value of density in the star region is far from vacuum. This is probably related to the very large deformations present in the exact solution.

5.3 Sonic point test problem

We solve the Riemann problem with the following initial data

$$\boldsymbol{W}_L = (0, 0, 0.8, 0, 0, 1, 0), \quad \boldsymbol{W}_R = (3, 0, 1, 0, 0, 1, 0), \tag{31}$$

and $x_0 = 0.55$. The structure of the solution is similar to that of the separation problem with an important difference that now the left rarefaction wave contains a sonic point:

$$\boldsymbol{W}(x,t) = \begin{cases} \boldsymbol{W}_L, & & (x-x_0)/t & < -10.5988, \\ \text{left rarefaction}, & -10.5988 < & (x-x_0)/t & < 0.4386, \\ \boldsymbol{W}_*, & 0.4386 < & (x-x_0)/t & < 4.1602 \\ \text{right rarefaction}, & 4.1602 < & (x-x_0)/t & < 7.6000, \\ \boldsymbol{W}_R, & & (x-x_0)/t & > 7.6000. \end{cases}$$

Here the star state is

$$\boldsymbol{W}_* = (2.299, 0, 1.254, 0, 0, 1, 0).$$

We run the schemes up to the output time $t = 0.04$ with CFL coefficient $CFL = 0.9$. Let us first discuss the results of Lax-Friedrichs and GFORCE fluxes shown on Fig. 5 for a mesh of 100 cells. For this problem GMUSTA-1 gives results which are very similar to the GFORCE scheme and are thus omitted. The results of the linearized and EVILIN-1 solvers are shown on Fig. 7 for three meshes: 100, 400 and 1600 cells. All methods produce a pronounced density deep in the star region. As expected, the linearized solver exhibits a large non-physical discontinuity at the sonic point, a so-called rarefaction shock, on all meshes, but away from it is quite accurate. The EVILIN-1 solver, however, avoids generating the rarefaction shock due to the GMUSTA predictor step. Overall, from Figs.

5, 7 we conclude that EVILIN-1 is the most accurate flux for this problem whereas the Lax-Friedrichs flux is most diffusive with a typical pairing of cells.

Given the size of the deep in the star region both in the symmetric separation and sonic point problems, one may naturally ask if the methods converge to the exact solution at all when the mesh is refined. To verify this numerically, we have carried out computations of the sonic point problem on a sequence of meshes. Fig. 6 shows the results of the GFORCE scheme on two meshes: 5000 and 20000 cells. As can be seen, the constant star region has indeed appeared in the numerical solution, but the spurious deep is still present. Therefore, the conclusion of this numerical convergence study is that convergence is exceedingly slow. We note that for this reason it is very difficult to obtain a reference solution for this test problems numerically, the exact solution being the only reliable option.

5.4 Stationary contact discontinuity

We solve the Riemann problem with initial data corresponding to a stationary contact discontinuity:

$$\begin{aligned} \boldsymbol{W}_L &= (0, 0, 1.156276139, 0.034688284, 0.093190648, 1.002195719, 0.001), \\ \boldsymbol{W}_R &= (0, 0, 1, 0.03, 0.02, 1, 0), \end{aligned} \tag{32}$$

and $x_0 = 0.5$. The exact solution is given by $\boldsymbol{W}(x,t) \equiv \boldsymbol{W}(x,0)$. We run the schemes up to the output time $t = 1$ on a mesh of 100 cells using a CFL coefficient $CFL = 0.9$. This corresponds to approximately 530 time steps.

Fig. 8 shows computed results for schemes with Lax-Friedrichs, GFORCE, linearized and EVILIN-1 fluxes. We see that the methods which do not resolve all the waves in the local Riemann problem solution (Lax-Friedrichs, GFORCE, GMUSTA) produce rather smeared profiles, the Lax-Friedrichs scheme being the worst. In particular, the computed normal velocity is not zero in the whole computational domain. Additionally, the computed normal stress σ_{11}, not shown in the figures, deviates from its exact value by about 5–10%. The linearized and EVILIN-1 solvers resolve the stationary contact discontinuity with one intermediate cell only. Since this intermediate cell is purely numerical the scheme produces visible over and undershoots in velocity and stresses across the numerical profile of the contact discontinuity. This is due to the fact that the numerical profile of internal energy across the discontinuity includes (non-physical) intermediate values. We also note that the EVILIN flux produces smaller velocity under and overshoots as compared to the linearized flux.

Fig. 9 shows results of the GMUSTA flux on the same mesh, for different numbers of stages. We see that the GMUSTA-1 flux is more accurate than both Lax-Friedrichs and

GFORCE fluxes. Next, when the number of stages increases the GMUSTA results seem to approach slowly a limiting profile, which is however different from the exact one.

5.5 Three-wave shock-tube problem

The initial data satisfying the compatibility conditions (7) is given by

$$\boldsymbol{W}_L = (0, 0, 0.95, 0, 0, 1, 0.001), \quad \boldsymbol{W}_R = (0, 0, 1, 0, 0, 1, 0), \tag{33}$$

and $x_0 = 0.5$. The structure of the solution consists of (from left to right) a left travelling rarefaction wave, a right-travelling contact discontinuity with velocity $S_M = 0.3948$ and a right-travelling shock wave with velocity $S_R = 5.5380$:

$$\boldsymbol{W}(x,t) = \begin{cases} \boldsymbol{W}_L, & & (x-x_0)/t & < -10.5988, \\ \text{left rarefaction}, & -6.3071 < & (x-x_0)/t & < -4.7331, \\ \boldsymbol{W}_{*L}, & -4.7331 < & (x-x_0)/t & < 0.3948, \\ \boldsymbol{W}_{*R}, & 0.3948 < & (x-x_0)/t & < 5.5380, \\ \boldsymbol{W}_R, & & (x-x_0)/t & > 5.5380. \end{cases}$$

Here the left and right star states are given by

$$\boldsymbol{W}_{*L} = (0.3948, 0, 1.0183, 0, 0, 1, 0.0010), \quad \boldsymbol{W}_{*R} = (0.3948, 0, 0.9287, 0, 0, 1, 0.00002668).$$

We run the schemes up to the output time $t = 0.06$ on a mesh of 100 cells and a CFL coefficient $CFL = 0.9$. Figs. 10 – 11 show computed results using the first-order scheme with different fluxes.

We first compare the results of the fluxes which do not recognize all the waves in the local Riemann problem solution, see Fig. 10. Overall, the least accurate is the scheme, which produces very smeared profiles of all quantities with very typical 'pairing' of cells. GFORCE and GMUSTA-1 fluxes are visibly more accurate for all waves. We note that these two fluxes are of virtually identical accuracy at the shock front and across the smooth rarefaction wave but differ for the contact discontinuity, for which GMUSTA-1 is more accurate.

The linearized solver produces the best resolution of all discontinuous fronts, especially for the contact discontinuity, see Fig. 11. This is explained by the fact that it recognizes all waves in the Riemann problem solution. However, there are also slight oscillations in the ρ and σ_{22} profiles near the contact discontinuity which somewhat degrades the results. The results of the EVILIN flux virtually coincide with those of the linearized

solver everywhere except near the contact discontinuity. Unfortunately, there are now visible oscillations in ρ and σ_{22} which are in fact more pronounced as compared to the linearized solver.

5.6 Five-wave shock-tube problem

Having assessed the performance of the fluxes on the purely one-dimensional problems with exact solution available we now solve a Riemann problem with solution in which all waves are non-trivial. The initial data is given by

$$\boldsymbol{W}_L = (0.0, 1.0, 0.95, 0.0, 0.05, 1., 0.001), \quad \boldsymbol{W}_R = (0.0, 0.0, 1.0, 0.0, 0.0, 1.0, 0.0) \tag{34}$$

and $x_0 = 0.5$. The structure of the solution consists of five waves (from left to right): two left-travelling rarefaction waves, a right-travelling contact discontinuity, a right-travelling rarefaction wave and a right-travelling shock wave. Since no exact solution is available, we generate a reference solution by running a high-order method on an exceedingly fine mesh of 10000 cells.

We run the schemes up to the output time $t = 0.06$ on a mesh of 200 cells and a CFL coefficient $CFL = 0.9$. Figs. 12 – 13 show computed results using the first-order scheme with different fluxes. Symbols correspond to numerical solution of the methods under discussion whereas the *reference solution* is plotted by the solid line. Overall, the differences in performance of the methods is similar to those observed in the simpler three-wave test problem. The centred Lax-Friedrichs flux produces the most diffusive results whereas the linearized Riemann solver is the most accurate. The EVILIN-1 flux is virtually identical to the linearized solver everywhere except for the contact discontinuity where it produces a visible undershoot in density ρ. For this test, the GFORCE and GMUSTA-1 fluxes represent a good compromise between accuracy and monotonicity.

So far we have run the methods with a CFL number close to unity. However, in some cases, e.g. when the system contains a source term or in multidimensional extensions of the methods, a smaller CFL number is required. It is therefore important to examine the effect of the choice of the CFL number on the accuracy of the fluxes. To accomplish this we have solved this test problem with a small Courant number CFL=0.1. Fig. 14 shows the results of Lax-Friedrichs, GFORCE and GMUSTA-1 fluxes. We see that the accuracy of the centred Lax-Friedrichs flux is degraded significantly by using such a small CFL number. The performance of the GFORCE flux is affected only slightly whereas the GMUSTA-1 flux is as accurate as for CFL=0.9 and is clearly superior to other two. The accuracy of two other fluxes, linearized and EVILIN-1, does not seem to be sensitive to the choice of CFL either.

6 Extension to higher order of accuracy

The presented fluxes can be used directly to construct high-order finite-volume schemes. Here we illustrate this in the frame of the state-of-art weighted essentially non-oscillatory (WENO) schemes with third-order Runge-Kutta time stepping. For a detailed description of the WENO schemes see [8, 6, 17] and references therein. Here we provide a brief description of the method.

Integrating (5) with respect to x over the volume and keeping the time variable t continuous we obtain the following semi-discrete finite-volume scheme which is in fact a system of ordinary differential equations (ODE):

$$\frac{d}{dt}\boldsymbol{U}_i(t) = -\frac{1}{\Delta x}\left(\boldsymbol{F}_{i+1/2} - \boldsymbol{F}_{i-1/2}\right) \equiv \boldsymbol{L}_i(\boldsymbol{U}), \tag{35}$$

where $\boldsymbol{U}_i(t)$ is the space average of the solution in the cell $[x_{i-1/2}, x_{i+1/2}]$ at time t and $\boldsymbol{F}_{i+1/2}$ is the numerical flux at $x = x_{i+1/2}$ and time t, that is

$$\boldsymbol{U}_i(t) = \frac{1}{\Delta x}\int_{x_{i-1/2}}^{x_{i+1/2}} \boldsymbol{U}(x,t)\,dx, \quad \boldsymbol{F}_{i+1/2} = \boldsymbol{F}(\boldsymbol{U}(x_{i+1/2},t)). \tag{36}$$

The numerical solution of (35) is advanced in time by means of the following third-order TVD Runge-Kutta method (here we dropped the index i)

$$\begin{aligned}
\boldsymbol{U}^{(n+1/3)} &= \boldsymbol{U}^n + \Delta t\,\boldsymbol{L}(\boldsymbol{U}^n),\\
\boldsymbol{U}^{(n+2/3)} &= \frac{3}{4}\boldsymbol{U}^n + \frac{1}{4}\boldsymbol{U}^{(n+1/3)} + \frac{1}{4}\Delta t\,\boldsymbol{L}(\boldsymbol{U}^{(n+1/3)}),\\
\boldsymbol{U}^{n+1} &= \frac{1}{3}\boldsymbol{U}^n + \frac{2}{3}\boldsymbol{U}^{(n+2/3)} + \frac{2}{3}\Delta t\,\boldsymbol{L}(\boldsymbol{U}^{(n+2/3)}).
\end{aligned} \tag{37}$$

The numerical flux at the cell boundary $x_{i+1/2}$ is defined as a function of left and right extrapolated values $\boldsymbol{U}^L_{i+1/2}$, $\boldsymbol{U}^R_{i+1/2}$:

$$\boldsymbol{F}_{i+1/2} = \boldsymbol{F}(\boldsymbol{U}_{i+1/2}(t)) = \boldsymbol{F}_{i+1/2}(\boldsymbol{U}^L_{i+1/2}, \boldsymbol{U}^R_{i+1/2}), \tag{38}$$

for which we use the fluxed described in this paper. The extrapolated values are obtained from cell averages by means of a high order essentially non-oscillatory polynomial reconstruction. In this paper we use the fifth order WENO reconstruction proposed in [6]. For a scalar function $q(x)$ the fifth order accurate left boundary extrapolated value $q^L_{i+1/2}$ in terms of cell averages q_i is defined as

$$q^L_{i+1/2} = \omega_0 v_0 + \omega_1 v_1 + \omega_2 v_2, \tag{39}$$

where v_k is the extrapolated value obtained from cell averages in the k^{th} stencil $S_k = (i-k, i-k+1, i-k+2)$ and ω_k, $k = 1, 2, 3$, are nonlinear WENO weights given by

$$\omega_k = \frac{\alpha_k}{\sum\limits_{l=0}^{3}\alpha_l}, \quad \alpha_0 = \frac{3}{10(\varepsilon+\beta_0)^2}, \quad \alpha_1 = \frac{3}{5(\varepsilon+\beta_1)^2}, \quad \alpha_2 = \frac{1}{10(\varepsilon+\beta_2)^2}.$$

Here a small parameter ε is introduced to avoid division by zero. A recommended value is $\varepsilon = 10^{-6}$. However, we find that setting $\varepsilon = 10^{-15}$ gives much better results. The expressions for the extrapolated values v_k and smoothness indicators β_k can be found in [6] and are thus omitted. The right value $q^R_{i+1/2}$ is obtained by symmetry. For systems the reconstruction is carried out in characteristic variables rather than conservative variables and (39) is applied to each characteristic field.

We run the scheme for the five-wave shock-tube problem (34) from the previous section a mesh of 200 cells and a CFL coefficient $CFL = 0.6$. Fig. 15 shows results computed using the GFORCE flux. Overall, the resolution of all waves is good without visible oscillations.

7 Conclusions

In this paper we have first constructed exact solutions to the Riemann problem for the equations of non-linear elasticity. Some of these solutions have then been proposed as test problems to assess the performance of numerical methods intended for solving the general initial-boundary value problem for the equations of non-linear elasticity. Then we have implemented some recently proposed numerical fluxes and have carried out a detailed and systematic assessment of the corresponding finite volume methods, both in their first-order and higher order modes using the WENO framework. The GFORCE and one-stage GMUSTA fluxes represent a good compromise between robustness and accuracy; their performance is distinctly better than that of the classical Lax-Friedrichs flux. The simple linearized Riemann solver works well for a restricted class of problems but has the usual difficulties of linearized Riemann solvers, such as lack of robustness generally, the computation of entropy-violating shocks, etc. The EVILIN flux represents an improvement over the linearized solver but for the severe test problems designed in this paper it also runs into similar difficulties to those of the simple linearized solver. GFORCE and GMUSTA are generally very robust and simple; their resolution of discontinuities approaches that of the linearized solver or EVILIN, particularly for fast-moving waves. Therefore the GFORCE and GMUSTA-1 fluxes represent a good choice for practical calculations in non-linear elasticity.

Acknowledgements

The first author acknowledges the financial support provided by the PRIN programme (2004-2006) of Italian Ministry of Education and Research (MIUR). The second author also acknowledges MIUR for the partial financial support provided during his stay as a

visiting professor at the Department of Civil and Environmental Engineering, University of Trento. The third author acknowledges the support of an EPSRC grant, as senior visiting fellow (Grant GR N09276) at the Isaac Newton Institute for Mathematical Sciences, University of Cambridge, UK, 2003.

References

[1] B. Einfeldt, C.D. Munz, P.L. Roe, and B. Sjogreen. On Godunov-type methods near low densities. *J. Comput. Phys.*, 92:273–295, 1991.

[2] S.K. Godunov. A finite difference method for the computation of discontinuous solutions of the equations of fluid dynamics. *Mat. Sbornik*, 47:357–393, 1959.

[3] S.K. Godunov and E.I. Romenski. Nonstationary equations of the nonlinear theory of elasticity in Euler coordinates. *J. Appl. Mech. Tech. Phys.*, 13(6):868–885, 1972.

[4] S.K. Godunov and E.I. Romenski. Thermodynamics, conservation laws, and symmetric forms of differential equations in mechanics of continuous media. In *Computational Fluid Dynamics Review 95*, pages 19–31. John Wiley, NY, 1995.

[5] S.K. Godunov and E.I. Romenski. *Elements of Continuum Mechanics and Conservation Laws*. Kluwer Academic/ Plenum Publishers, 2003.

[6] G.S. Jiang and C.W. Shu. Efficient implementation of weighted ENO schemes. *J. Comput. Phys.*, 126:202–212, 1996.

[7] A.G. Kulikovskii, N. V. Pogorelov, and A. Yu. Semenov. *Mathematical Aspects of Numerical Solution of Hyperbolic Systems*. Chapman and Hall, 2002. Monographs and Surveys in Pure and Applied Mathematics, Vol. 118.

[8] X.D. Liu, S. Osher, and T. Chan. Weighted essentially non-oscillatory schemes. *J. Comput. Phys.*, 115:200–212, 1994.

[9] L.A. Merzhievskii and A.D. Resnyansky. Shock-wave processes in metals. *Combustion, Explosion, and Shock Waves*, 20(5):580–587, 1984.

[10] L.A. Merzhievskii and A.D. Resnyansky. Numerical analysis for the abnormality of protective properties of a thin shield under oblique impact. *Combustion, Explosion, and Shock Waves*, 29(6):744–749, 1994.

[11] G.H. Miller. An iterative Riemann solver for system of conservation laws, with application to hyperelastic solid mechanics. *J. Comput. Phys*, 193:198–225, 2003.

[12] G.H. Miller and P. Colella. A high-order Eulerian Godunov method for elastic-plastic flow in solids. *J. Comput. Phys*, 167:131–176, 2001.

[13] B.J. Plohr and D.H. Sharp. A conservative formulation for plasticity. *Adv. Appl. Math.*, 462-493:429–466, 1992.

[14] L. Quartapelle, L. Castelletti, A. Guardone, and G. Quaranta. Solution of the Riemann problem of classical gasdynamics. *J. Comput. Phys.*, 190(1):118–140, 2003.

[15] E. Romenski. Conservation laws and the symmetric form of equations of nonlinear elasticity theory. In *Boundary Value Problems for Partial Differential Equations, Proc. Sobolev Seminar*, volume 1, pages 132–43. Akad. Nauk USSR, Sib. Otd., Inst. Mat. Novosibirsk, 1984. in Russian.

[16] E. Romenski. Numerical method for 2d equations of nonlinear elasto-plastic Maxwell media. In *Proc. Inst. Math. Akad. Nauk USSR, Sib. Otd.*, volume 18, pages 83–100, 1990. in Russian.

[17] J. Shi, C. Hu, and C.-W. Shu. A technique for treating negative weights in WENO schemes. *J. Comput. Phys.*, 175:108–127, 2002.

[18] V.A. Titarev and E.F. Toro. MUSTA schemes for multi-dimensional hyperbolic systems: analysis and improvements. *International Journal for Numerical Methods in Fluids*, 49(2):117–147, 2005.

[19] E.F. Toro. On Glimm-related schemes for conservation laws. *Technical Report MMU-9602, Department of Mathematics and Physics, Manchester Metropolitan University, UK.*, 1996.

[20] E.F. Toro. *Riemann solvers and numerical methods for fluid dynamics.* Springer-Verlag, 1999. Second Edition.

[21] E.F. Toro. Multi-stage predictor-corrector fluxes for hyperbolic equations. *Preprint NI03037-NPA. Isaac Newton Institute for Mathematical Sciences, University of Cambridge, UK*, 2003.

[22] E.F. Toro. Riemann solvers with evolved initial conditions. Int. J. Numer. Meth. Fluids, to appear.

[23] E.F. Toro and S.J. Billett. Centred TVD schemes for hyperbolic conservation laws. *IMA J. Numerical Analysis*, 20(1):47–79, 2000.

[24] E.F. Toro and V.A. Titarev. MUSTA schemes for systems of conservation laws. *Preprint NI04033-NPA. Isaac Newton Institute for Mathematical Sciences, University of Cambridge, UK*, 2004. to appear in J. Comp. Phys.

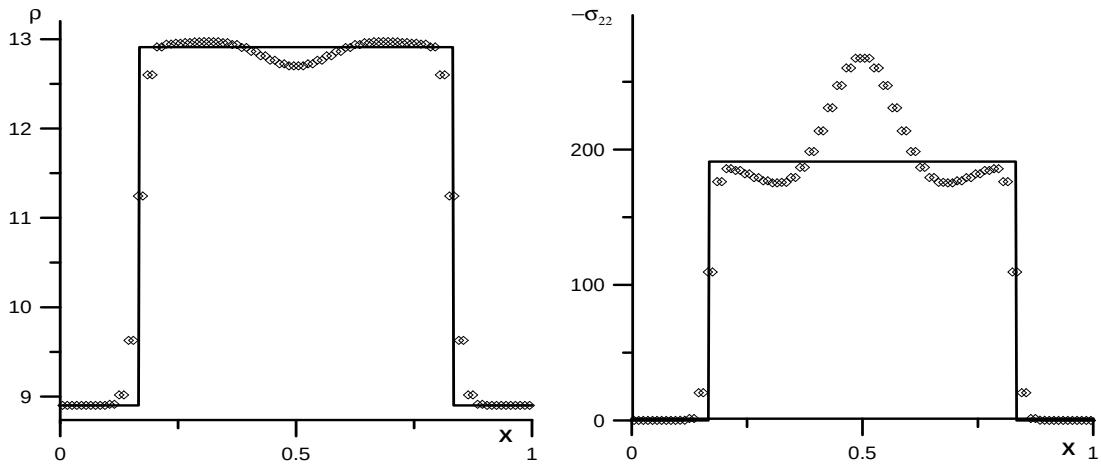

Figure 1: Impact problem. First-order scheme with the Lax-Friedrichs flux. The solid line represents the exact solution.

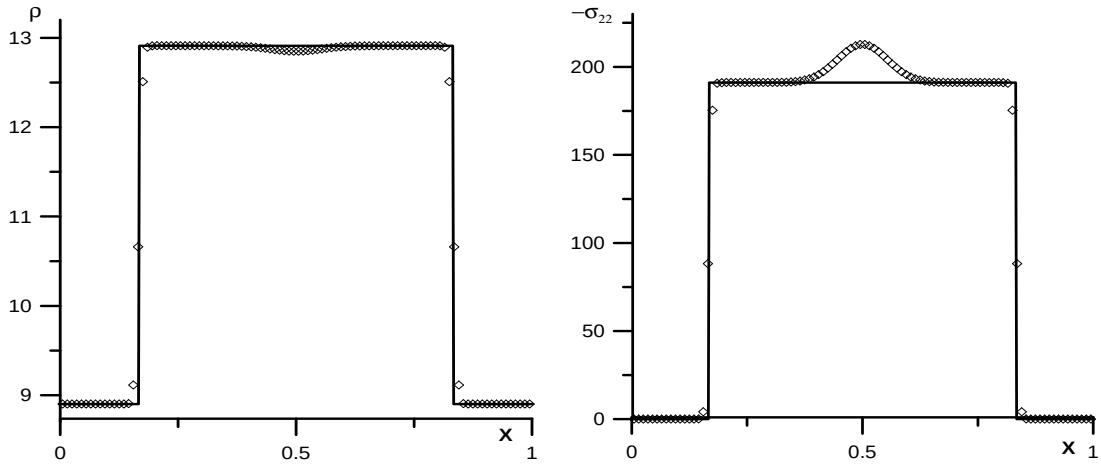

Figure 2: Impact problem. First-order scheme with the GFORCE flux. The solid line represents the exact solution.

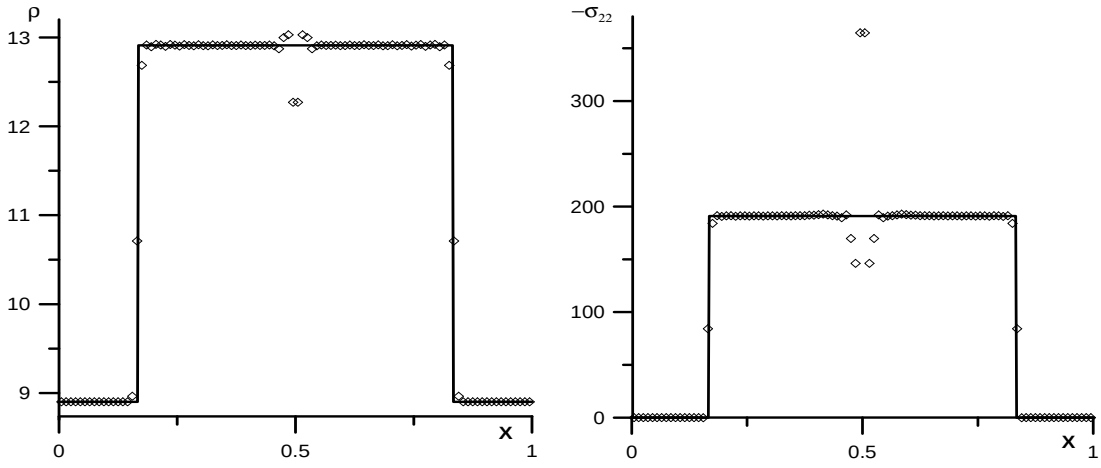

Figure 3: Impact problem. First-order scheme with the EVILIN flux. The solid line represents the exact solution.

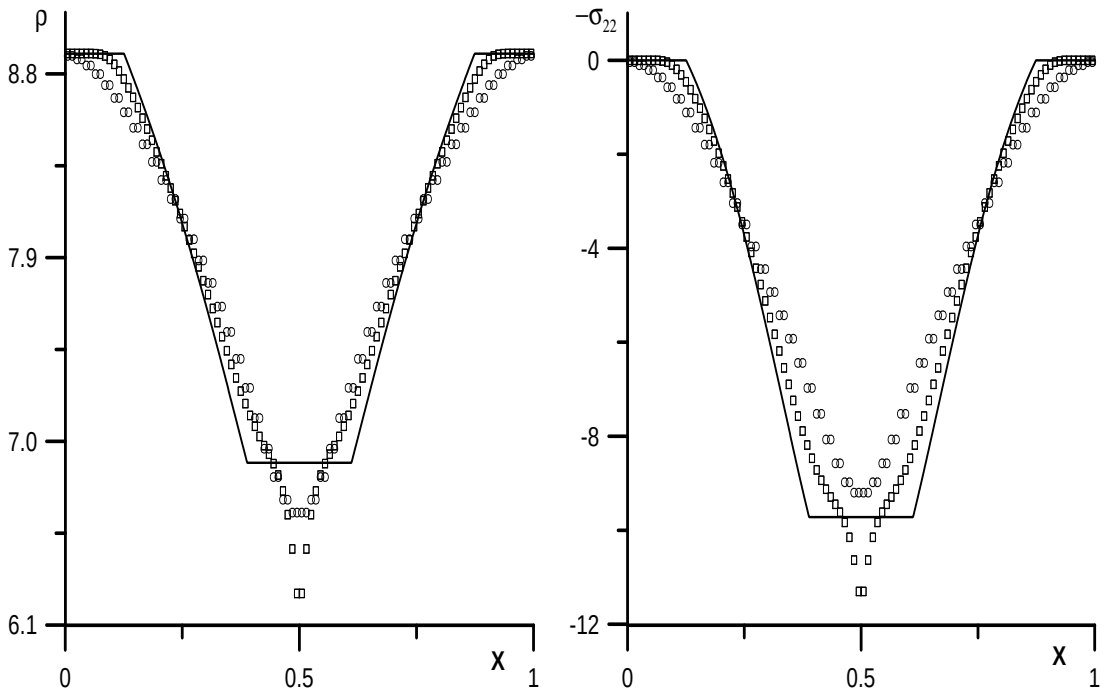

Figure 4: Separation problem. First-order scheme with the Lax-Friedrichs and GMUSTA-1 fluxes. The solid line represents the exact solution.

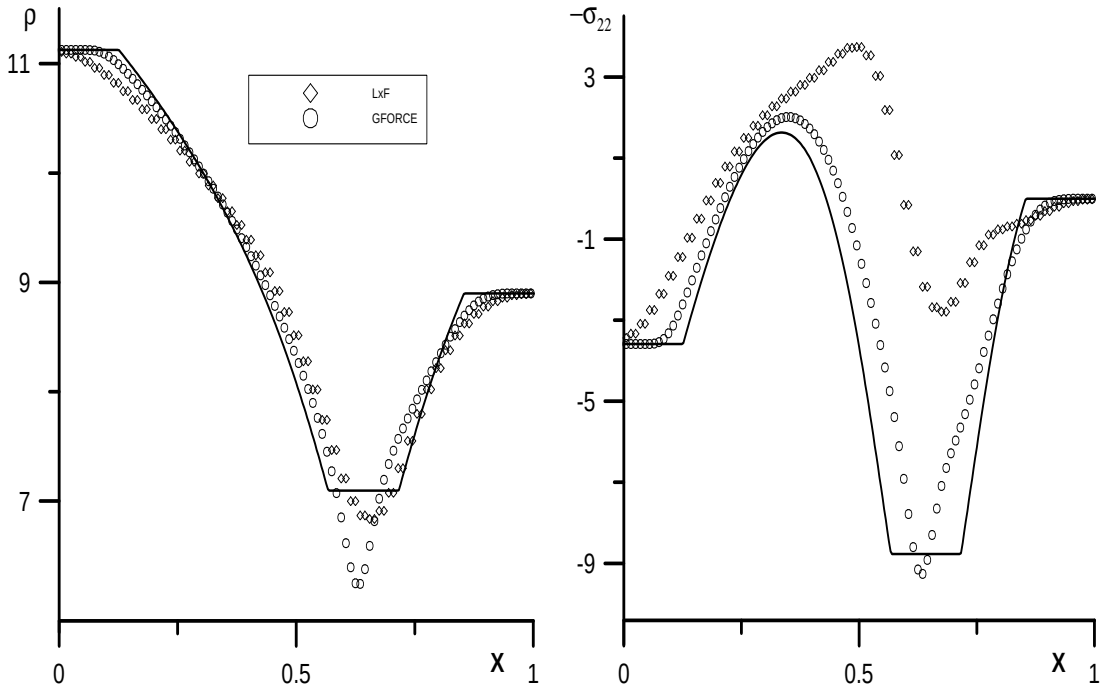

Figure 5: Sonic point problem. First-order scheme with the Lax-Friedrichs and GFORCE fluxes. The solid line represents the exact solution.

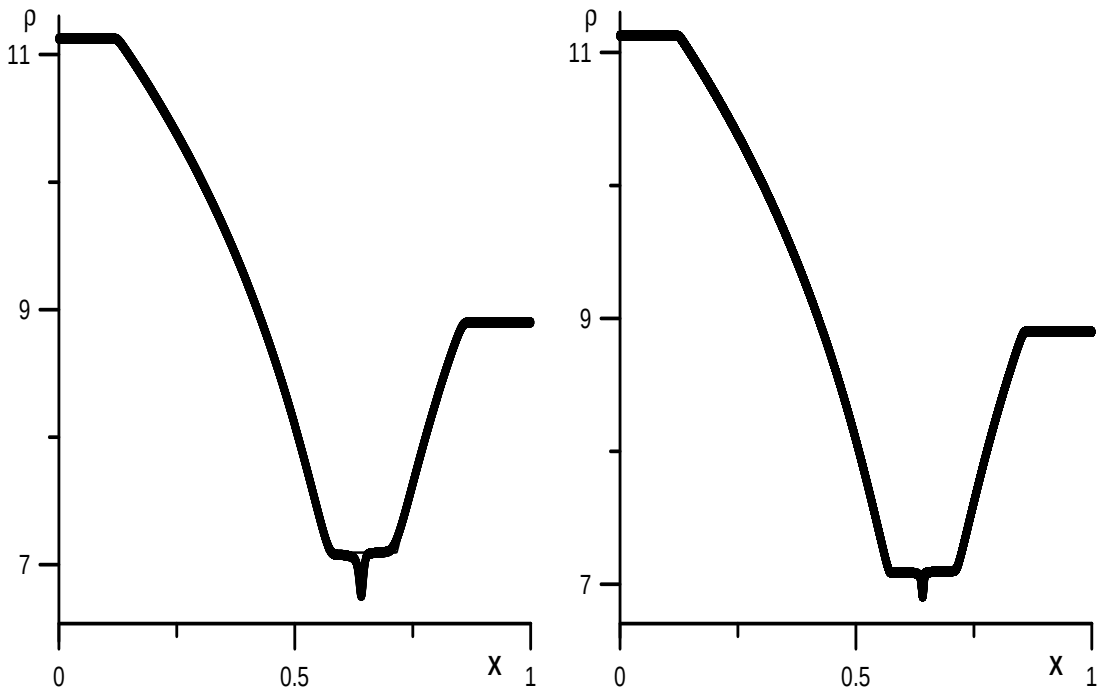

Figure 6: Sonic point problem. GFORCE flux and mesh of 5000 (left) and 20000 (right) cells. The solid line represents the exact solution.

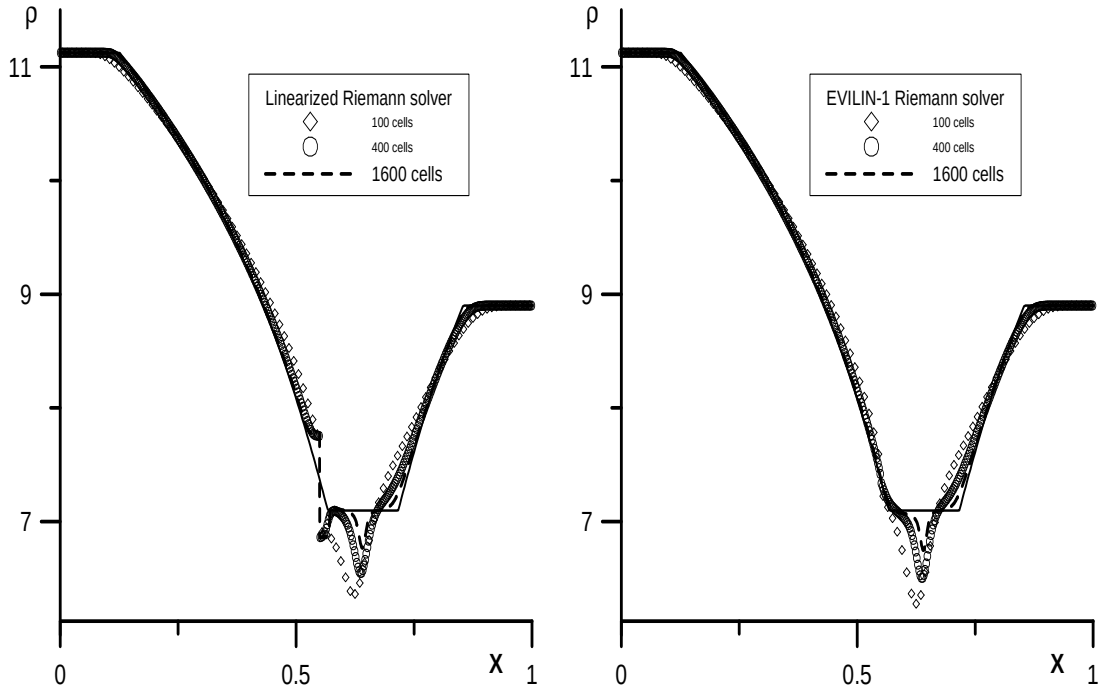

Figure 7: Sonic point problem. First-order scheme with the linearized and EVILIN-1 fluxes. The solid line represents the exact solution.

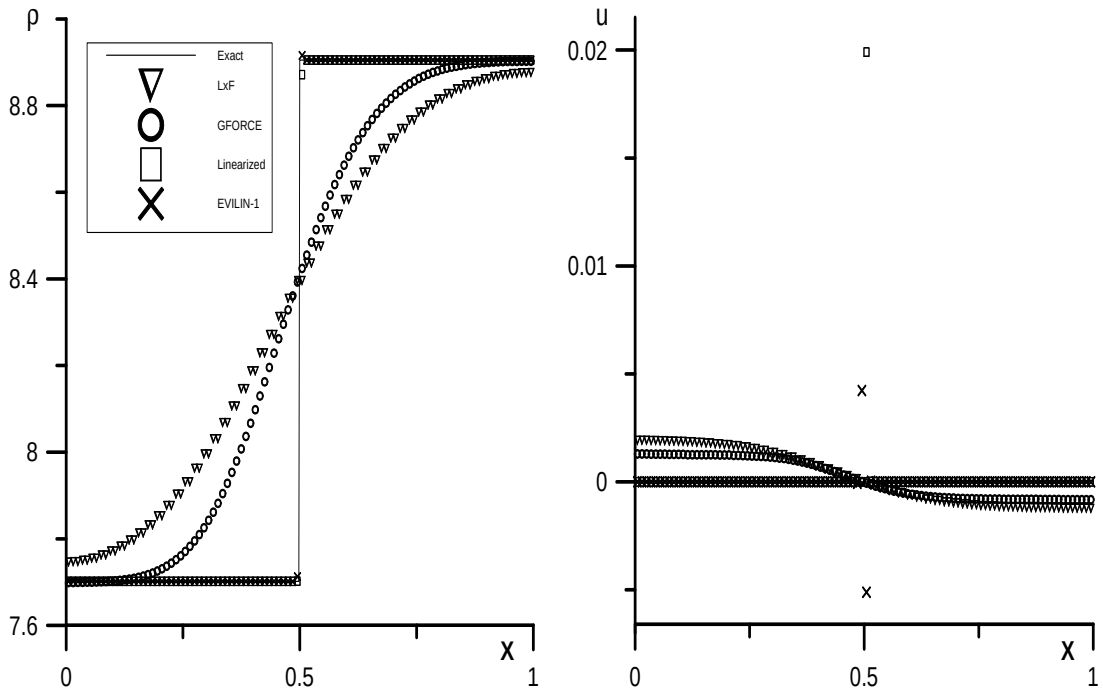

Figure 8: Stationary contact discontinuity. First-order scheme with Lax-Friedrichs, GFORCE, linearized and EVILIN-1 fluxes. The solid line represents the exact solution.

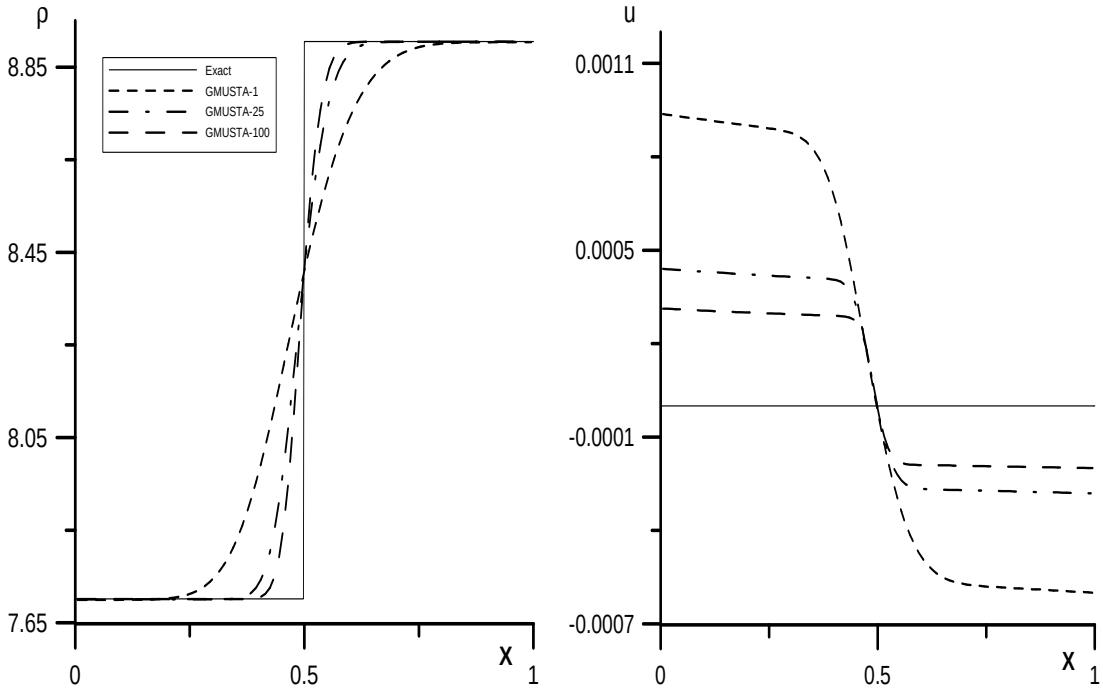

Figure 9: Stationary contact discontinuity. First-order scheme with the GMUSTA flux and different number of stages. The solid line represents the exact solution.

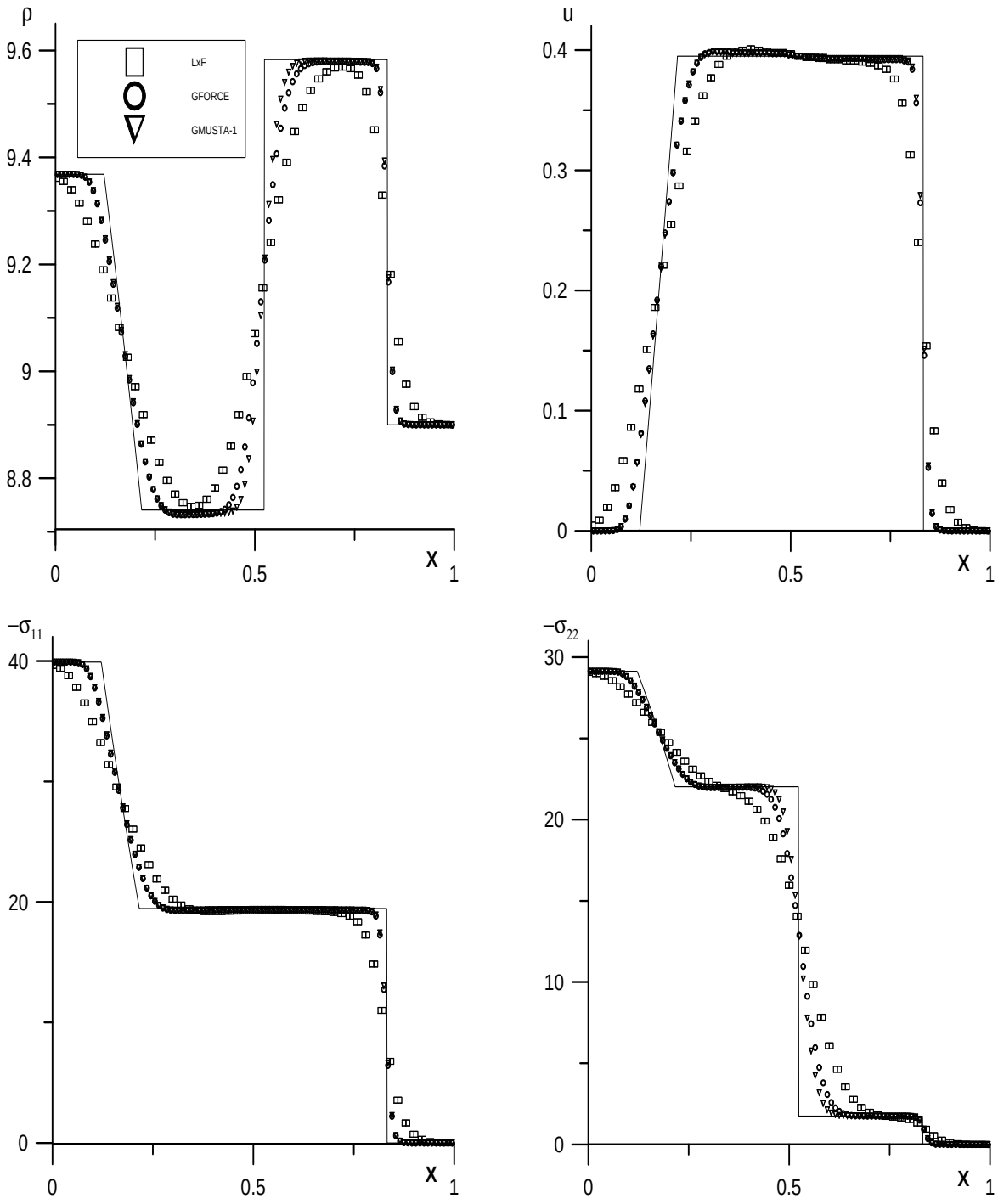

Figure 10: Three-wave shock-tube problem. First-order scheme with the Lax-Friedrichs, GFORCE and GMUSTA-1 fluxes. The solid line represents the exact solution.

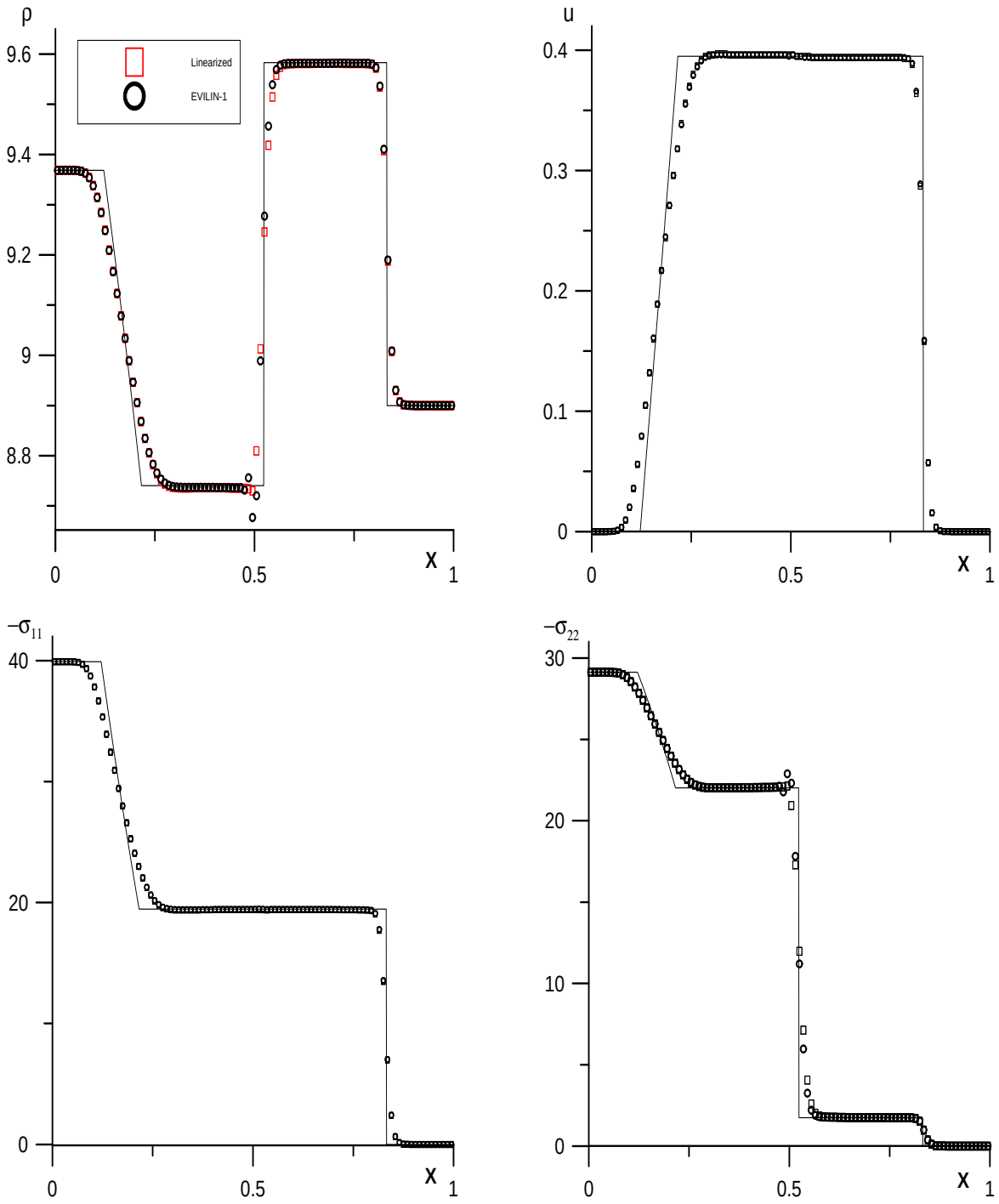

Figure 11: Three-wave shock-tube problem. First-order scheme with the linearized and EVILIN-1 fluxes. The solid line represents the exact solution.

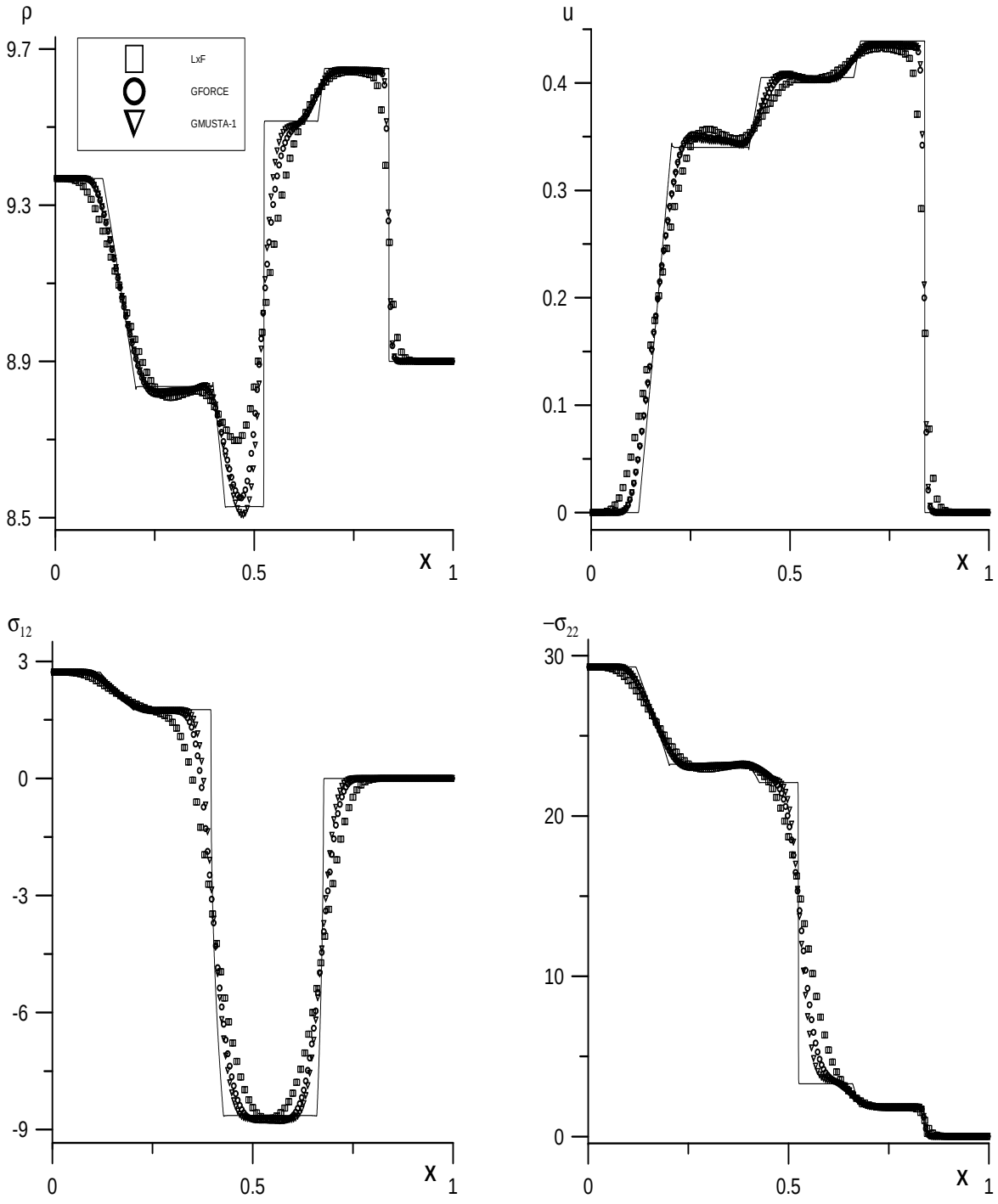

Figure 12: Five-wave shock-tube problem. First-order scheme with the Lax-Friedrichs, GFORCE and GMUSTA-1 fluxes. The solid line represents the fine-mesh reference solution.

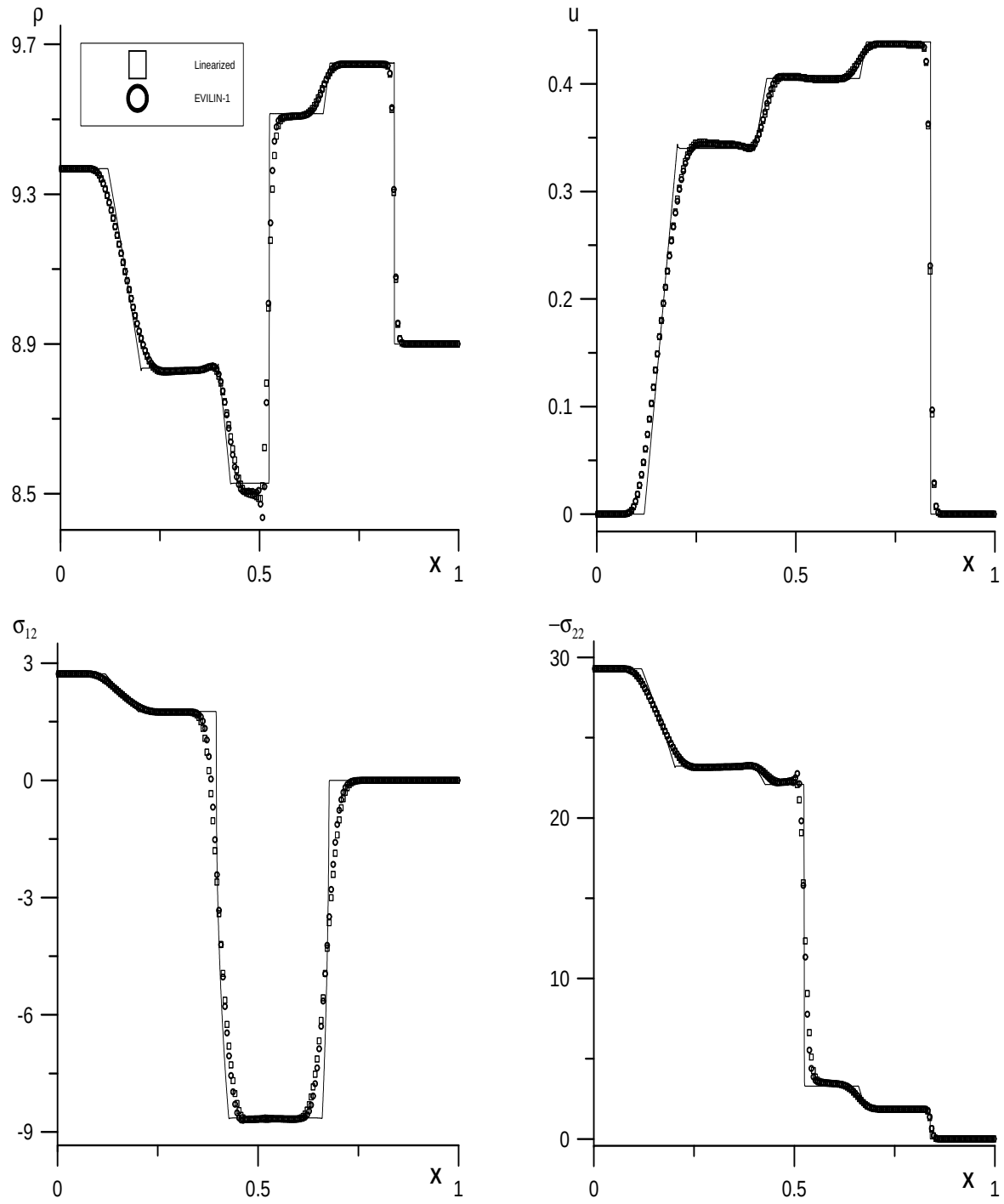

Figure 13: Five-wave shock-tube problem. First-order scheme with the linearized and EVILIN-1 fluxes. The solid line represents the fine-mesh reference solution.

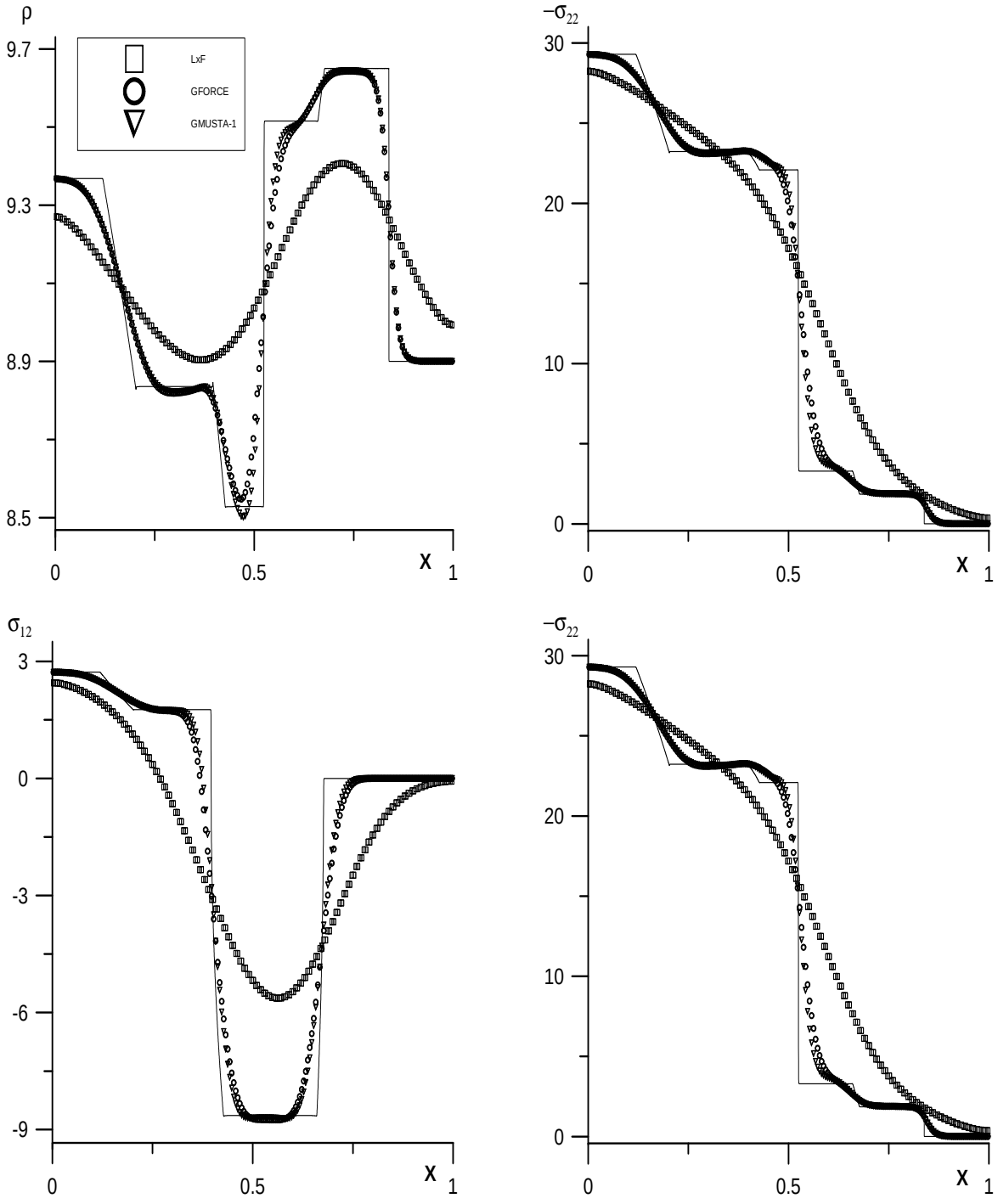

Figure 14: Five-wave shock-tube problem. First-order scheme with the Lax-Friedrichs, GFORCE and GMUSTA-1 fluxes. Small Courant number CFL=0.1. The solid line represents the fine-mesh reference solution.

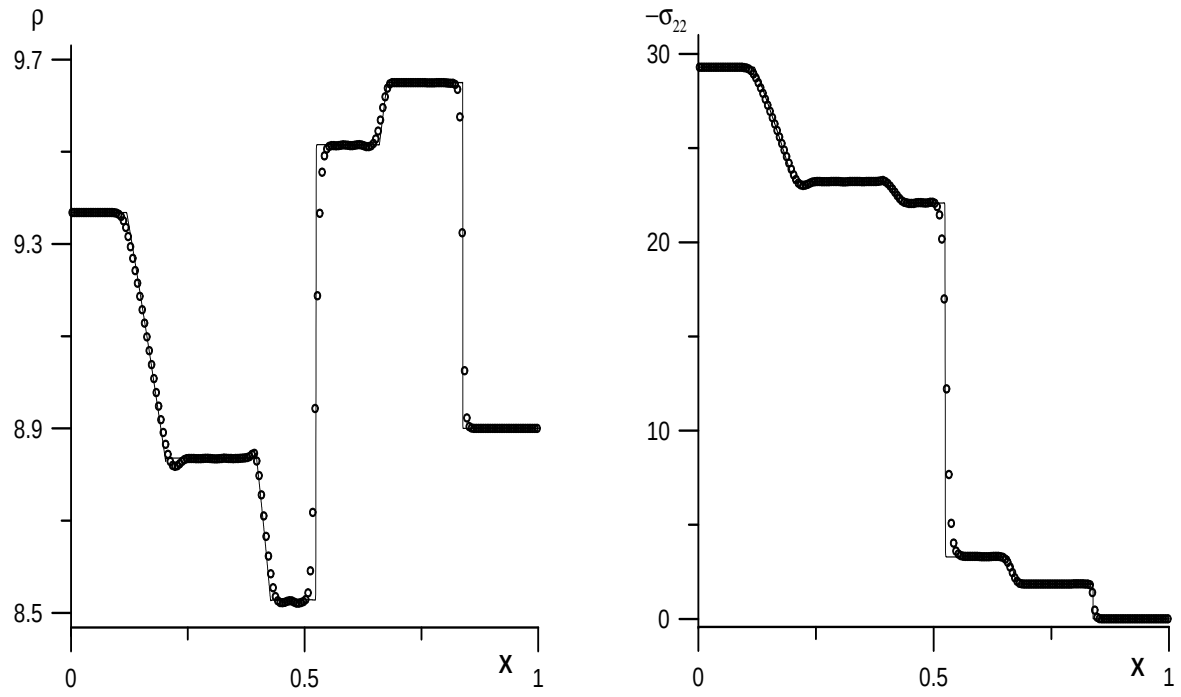

Figure 15: Five-wave shock-tube problem. WENO with the GFORCE flux. The solid line represents the fine-mesh reference solution.